Supplementary Information for

Predictions of Attainable Compositions of Layered Quaternary *i*-MAB Phases and solid solution MAB phases

Martin Dahlqvist*, Johanna Rosen*

Thin Film Physics, Department of Physics, Chemistry and Biology (IFM), Linköping University, SE-581 83 Linköping, Sweden

* corresponding author: martin.dahlqvist@liu.se; johanna.rosen@liu.se

This PDF file contains:

Schematic illustration of considered magnetic configurations for quaternary chemically ordered *i*-MAB phases (Figure S1) and quaternary solid solution MAB phases (Figure S2).
Convergence test for plane-wave energy cut-off and k-point density (Figure S3).
Experimentally known ternary MAB phases (Table S1), quaternary solid solution MAB phases (Table S2) and quaternary chemically ordered *i*-MAB phases (Table S3).
Calculated thermodynamic stability of quaternary MAB phases evaluated at 0 K (Figure S4).
Theoretically predicted stable quaternary MAB phases at 2000 K (Table S4-S6).
Dynamical stability calculated for thermodynamically stable *i*-MAB phases (Figure S5-S43).
Atomic radius and electronegativity for considered *M* and *A* elements (Table S7).
Calculated density of states, crystal overlap Hamilton population integrated crystal overlap Hamilton population for selected *i*-MAB phases (Figure S44-S48).
Calculated electronic bend-structures for selected *i*-MAB phases (Figure S49-S57).
Details for retrieving mechanical properties and corresponding results (Table S8 and Figure S58).

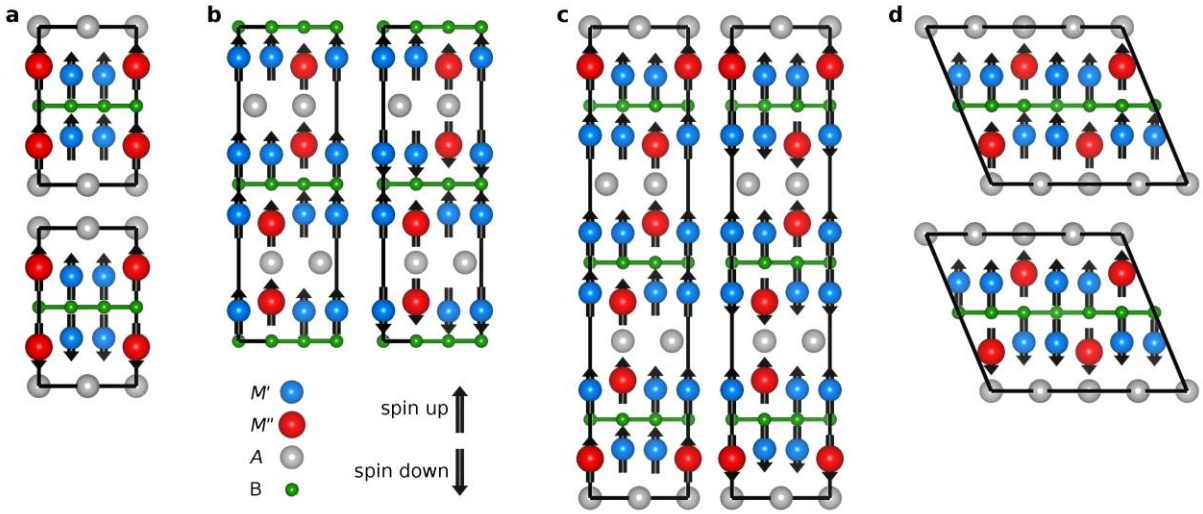

Figure S1. Schematic illustration of considered spin configurations for *i*-MAB phases with space group symmetry (a) $P\bar{6}2m$, (b) $P\bar{6}2c$, (c) $R\bar{3}m$, and (d) $C2$.

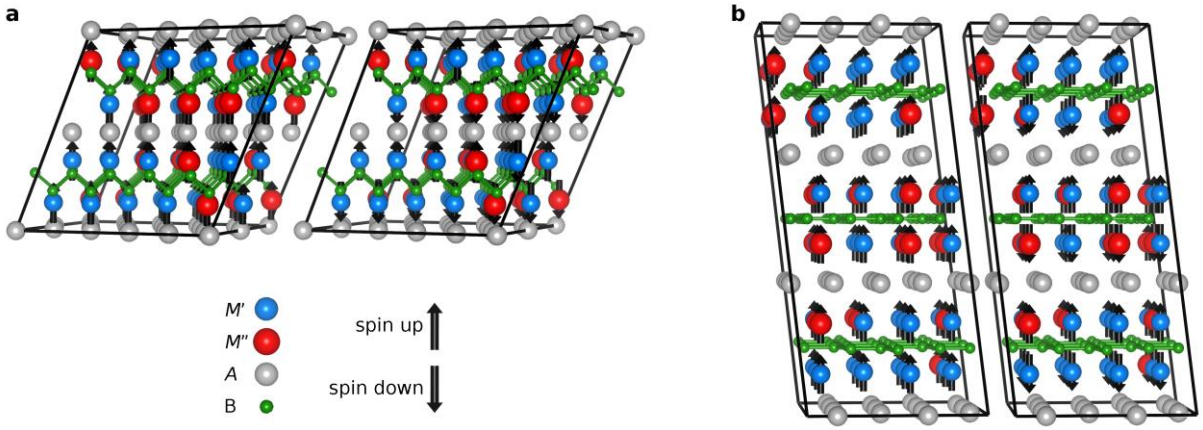

Figure S2. Schematic illustration of considered spin configurations for disordered solid solution MAB phases with space group symmetry (a) $Cmmm$ and (b) $P\bar{6}m2$.

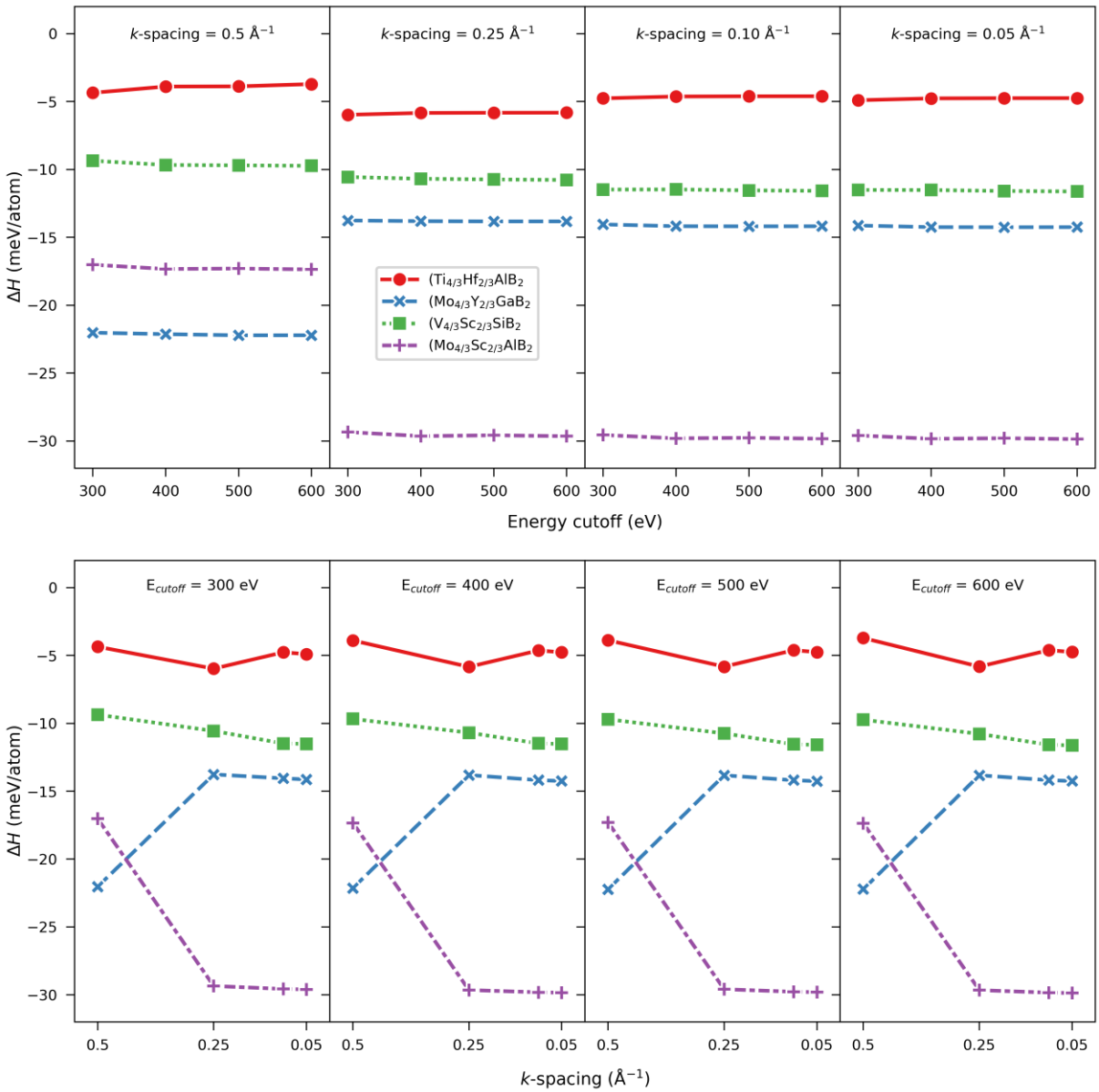

Figure S3. Demonstration for convergence of formation enthalpy ΔH_{cp} for four different *i*-MAB phases with space group $R\bar{3}m$. Top panels show ΔH_{cp} as function of plane wave energy cutoff using four different *k*-point densities for the *i*-MAB phase and its competing phases. Bottom panels show ΔH_{cp} as function of *k*-point density for different plane wave energy cutoffs for the *i*-MAB phase and its competing phases. Using a plane wave energy cutoff pf 400 eV combined with a *k*-point density of 0.05 Å^{-1} ensures ΔH_{cp} values within less than 0.5 meV/atom as compared to using larger cutoff energies or denser *k*-point meshes.

Table S1. Experimentally reported ternary M_2AB_2 phases.

Phase	Symmetry	References
Cr_2AlB_2	*Cmmm*	1-3
Mn_2AlB_2	*Cmmm*	1-5
Fe_2AlB_2	*Cmmm*	2, 3, 6, 7
Ti_2InB_2	$P\bar{6}m2$	8

Table S2. Experimentally reported quaternary solid solution MAB phases with *M*-site chemical disorder.

Phase	Symmetry	References
$(Mn_{0.67}Fe_{0.33})_2AlB_2$	*Cmmm*	3
$(Fe_{0.67}Mn_{0.33})_2AlB_2$	*Cmmm*	3
$(Cr_{0.67}Mn_{0.33})_2AlB_2$	*Cmmm*	9
$(Mn_{0.67}Cr_{0.33})_2AlB_2$	*Cmmm*	9

Table S3. Experimentally reported quaternary MAB phases with *M*-site chemical order (*i*-MAB)

Phase	Symmetry	References
$Mo_{4/3}Sc_{2/3}AlB_2$	$R\bar{3}m$	10
$Mo_{4/3}Y_{2/3}AlB_2$	$R\bar{3}m$	10

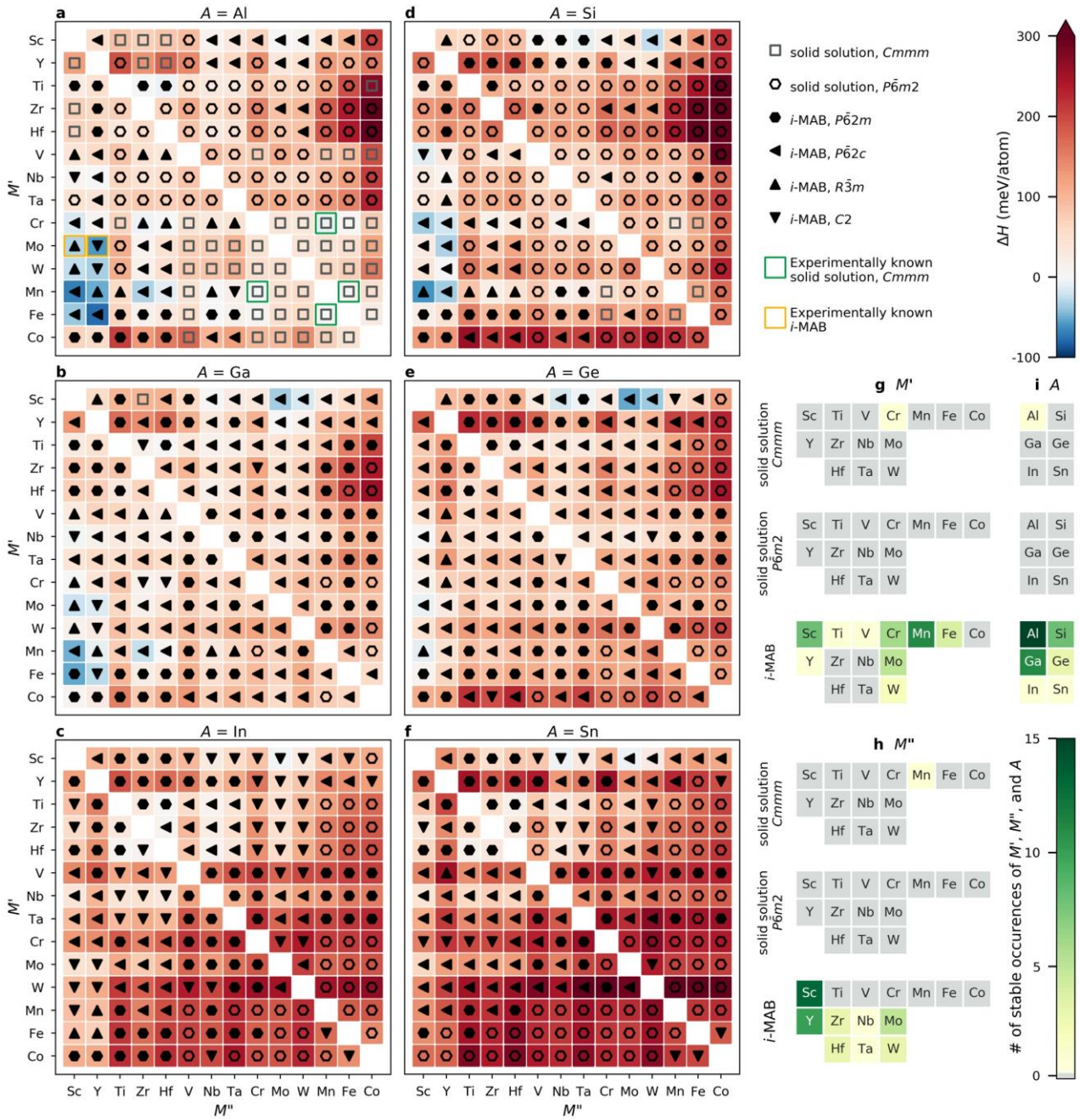

Figure S4. (a-f) Calculated formation enthalpy ΔH (order) or and Gibbs free energy of formation (solid solution) at 0 K for A = Al, Ga, In, Si, Ge, and Sn. Number of atomic elements in stable *i*-MAB and solid solution MAB phases for (g) *M´*, (h) *M´´*, and (i) *A*.

Table S4. Experimentally reported and theoretically predicted quaternary chemically ordered i-MAB phases, categorized by the calculated thermodynamic stability. The unit for $\Delta H_{i\text{-MAB}}$ and $\Delta G_{\text{solid solution}}$ is in meV/atom. Dynamically unstable *i*-MAB phases are marked with *.

Phase	**Stability criteria**	**Experimentally reported and here predicted**	**Predicted**
i-MAB, chemical order	$\Delta H_{o\text{-MAB}} < 0$	$Mo_{4/3}Sc_{2/3}AlB_2$ [10]	$Ti_{4/3}Hf_{2/3}AlB_2$
$M'_{4/3}M''_{2/3}AB_2$	$\Delta G_{\text{solid solution}} > \Delta H_{i\text{-MAB}}$	$Mo_{4/3}Y_{2/3}AlB_2$ [10]	$Cr_{4/3}Sc_{2/3}AlB_2$
			$Cr_{4/3}Zr_{2/3}AlB_2$
			$Cr_{4/3}Hf_{2/3}AlB_2$
			$W_{4/3}Sc_{2/3}AlB_2$
			$W_{4/3}Y_{2/3}AlB_2$
			$Mn_{4/3}Sc_{2/3}AlB_2$
			$Mn_{4/3}Y_{2/3}AlB_2$
			$Mn_{4/3}Zr_{2/3}AlB_2$
			$Mn_{4/3}Hf_{2/3}AlB_2$
			$Mn_{4/3}Nb_{2/3}AlB_2$
			$Fe_{4/3}Sc_{2/3}AlB_2$
			$Fe_{4/3}Y_{2/3}AlB_2$
			$Sc_{4/3}Mo_{2/3}GaB_2$*
			$Sc_{4/3}W_{2/3}GaB_2$*
			$Y_{4/3}Mo_{2/3}GaB_2$
			$Cr_{4/3}Sc_{2/3}GaB_2$
			$Mo_{4/3}Sc_{2/3}GaB_2$
			$Mo_{4/3}Y_{2/3}GaB_2$
			$Mn_{4/3}Sc_{2/3}GaB_2$
			$Mn_{4/3}Y_{2/3}GaB_2$
			$Mn_{4/3}Zr_{2/3}GaB_2$
			$Fe_{4/3}Sc_{2/3}GaB_2$
			$Fe_{4/3}Y_{2/3}GaB_2$
			$Sc_{4/3}Mo_{2/3}InB_2$
			$Sc_{4/3}Ta_{2/3}SiB_2$
			$Sc_{4/3}W_{2/3}SiB_2$*
			$V_{4/3}Sc_{2/3}SiB_2$
			$Cr_{4/3}Sc_{2/3}SiB_2$
			$Cr_{4/3}Y_{2/3}SiB_2$
			$Mo_{4/3}Y_{2/3}SiB_2$
			$Mn_{4/3}Sc_{2/3}SiB_2$
			$Mn_{4/3}Y_{2/3}SiB_2$
			$Sc_{4/3}Mo_{2/3}GeB_2$
			$Sc_{4/3}W_{2/3}GeB_2$
			$Mn_{4/3}Sc_{2/3}GeB_2$
			$Sc_{4/3}Mo_{2/3}SnB_2$

Table S5. Theoretically predicted quaternary disordered solid solution MAB phases with $P\bar{6}m2$ symmetry. The unit for $\Delta G_{\text{solid solution}}$ is in meV/atom.

Phase	**Stability criteria**	**Experimentally reported and here predicted**	**Predicted**
$P\bar{6}m2$, solid solution $(M'_{0.67}M''_{0.33})_2AB_2$	$\Delta G_{\text{solid solution}} \leq 0$ $\Delta G_{\text{solid solution}} < \Delta H_{i\text{-MAB}}$	N/A	$(Ti_{0.67}Nb_{0.33})_2AlB_2$ $(Ti_{0.67}Ta_{0.33})_2AlB_2$ $(Sc_{0.67}Nb_{0.33})_2GaB_2$ $(Ti_{0.67}Hf_{0.33})_2GaB_2$ $(Ti_{0.67}Nb_{0.33})_2GaB_2$ $(Ti_{0.67}Ta_{0.33})_2GaB_2$ $(Hf_{0.67}Nb_{0.33})_2GaB_2$ $(Nb_{0.67}Sc_{0.33})_2GaB_2$ $(Nb_{0.67}Ti_{0.33})_2GaB_2$ $(Nb_{0.67}Hf_{0.33})_2GaB_2$ $(Nb_{0.67}Ta_{0.33})_2GaB_2$ $(Nb_{0.67}Mo_{0.33})_2GaB_2$ $(Sc_{0.67}Nb_{0.33})_2InB_2$ $(Ti_{0.67}Zr_{0.33})_2InB_2$ $(Ti_{0.67}Hf_{0.33})_2InB_2$ $(Ti_{0.67}Nb_{0.33})_2InB_2$ $(Ti_{0.67}Ta_{0.33})_2InB_2$ $(Zr_{0.67}Ti_{0.33})_2InB_2$ $(Zr_{0.67}Hf_{0.33})_2InB_2$ $(Zr_{0.67}Nb_{0.33})_2InB_2$ $(Hf_{0.67}Ti_{0.33})_2InB_2$ $(Hf_{0.67}Zr_{0.33})_2InB_2$ $(Hf_{0.67}Nb_{0.33})_2InB_2$ $(Nb_{0.67}Ti_{0.33})_2InB_2$ $(Sc_{0.67}Nb_{0.33})_2GeB_2$ $(Sc_{0.67}Ta_{0.33})_2GeB_2$ $(Ti_{0.67}Ta_{0.33})_2GeB_2$ $(Nb_{0.67}Sc_{0.33})_2GeB_2$ $(Nb_{0.67}Mo_{0.33})_2GeB_2$ $(Mo_{0.67}Sc_{0.33})_2GeB_2$ $(Sc_{0.67}Nb_{0.33})_2SnB_2$ $(Ti_{0.67}Hf_{0.33})_2SnB_2$ $(Ti_{0.67}Nb_{0.33})_2SnB_2$ $(Zr_{0.67}Hf_{0.33})_2SnB_2$ $(Hf_{0.67}Ti_{0.33})_2SnB_2$ $(Hf_{0.67}Zr_{0.33})_2SnB_2$ $(Hf_{0.67}Nb_{0.33})_2SnB_2$

Table S6. Experimentally reported and theoretically predicted quaternary disordered solid solution MAB phases with *Cmmm* symmetry. The unit for $\Delta G_{\text{solid solution}}$ is in meV/atom.

Phase	**Stability criteria**	**Experimentally reported and here predicted**	**Predicted**
Cmmm, solid solution $(M'_{0.67}M''_{0.33})_2AB_2$	$\Delta G_{\text{solid solution}} \leq 0$ $\Delta G_{\text{solid solution}} < \Delta H_{i\text{-MAB}}$	$(Mn_{0.67}Fe_{0.33})_2AlB_2$ [3] $(Fe_{0.67}Mn_{0.33})_2AlB_2$ [3] $(Cr_{0.67}Mn_{0.33})_2AlB_2$ [9] $(Mn_{0.67}Cr_{0.33})_2AlB_2$ [9]	$(Cr_{0.67}V_{0.33})_2AlB_2$ $(Cr_{0.67}Mo_{0.33})_2AlB_2$ $(Cr_{0.67}W_{0.33})_2AlB_2$ $(Cr_{0.67}Fe_{0.33})_2AlB_2$ $(Mo_{0.67}Cr_{0.33})_2AlB_2$ $(Mo_{0.67}W_{0.33})_2AlB_2$ $(Mn_{0.67}V_{0.33})_2AlB_2$ $(Fe_{0.67}Cr_{0.33})_2AlB_2$ $(Fe_{0.67}Co_{0.33})_2AlB_2$ $(Co_{0.67}Fe_{0.33})_2AlB_2$ $(Cr_{0.67}Mn_{0.33})_2SiB_2$

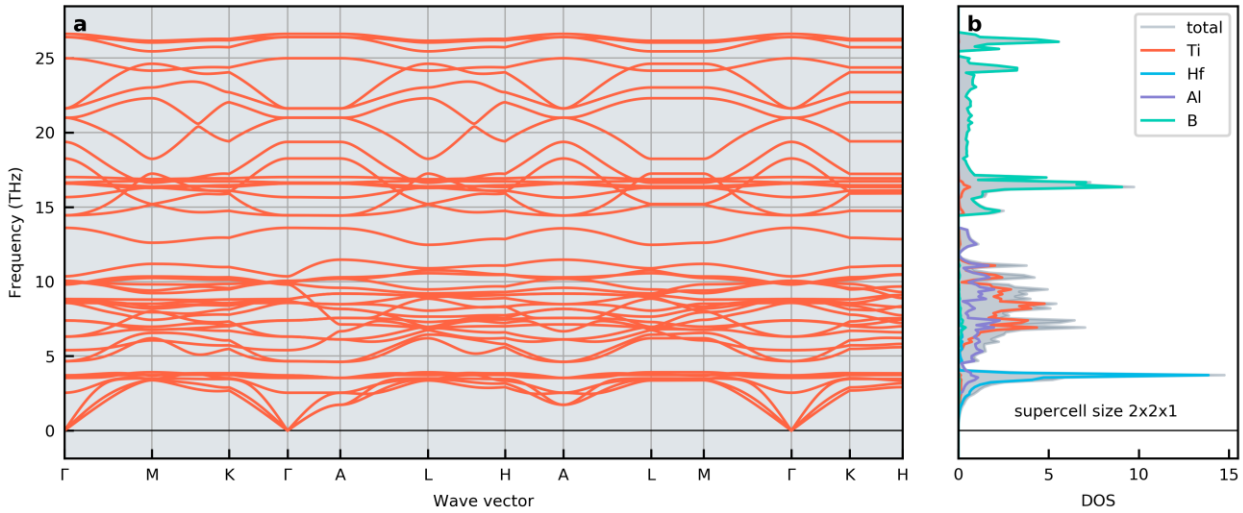

Figure S5. Phonon dispersion and phonon DOS for $Ti_{4/3}Hf_{2/3}AlB_2$ with $P\bar{6}2m$ symmetry.

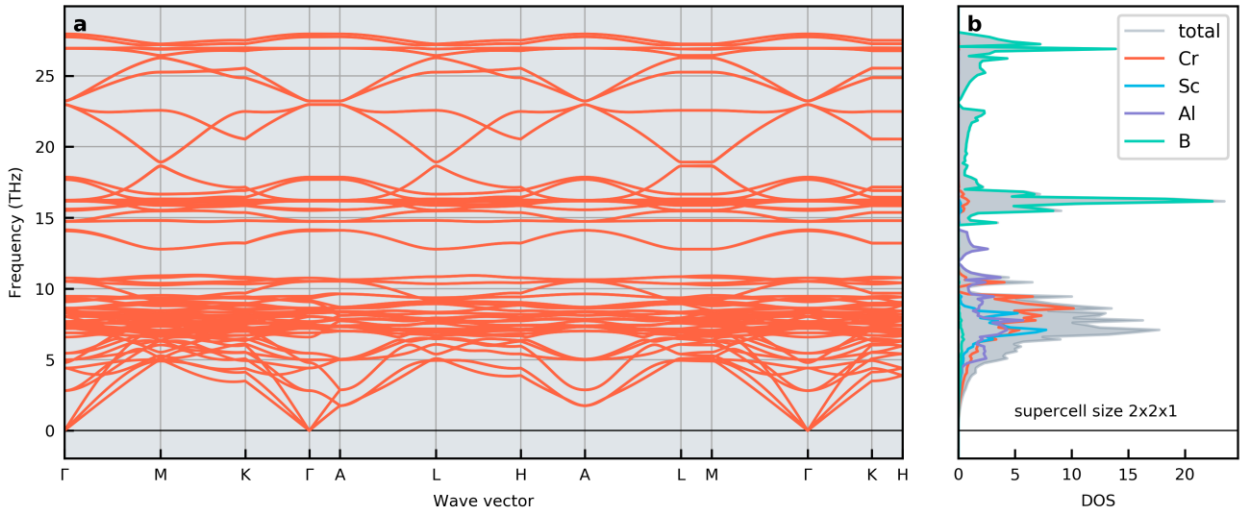

Figure S6. Phonon dispersion and phonon DOS for $Cr_{4/3}Sc_{2/3}AlB_2$ with $P\bar{6}2c$ symmetry.

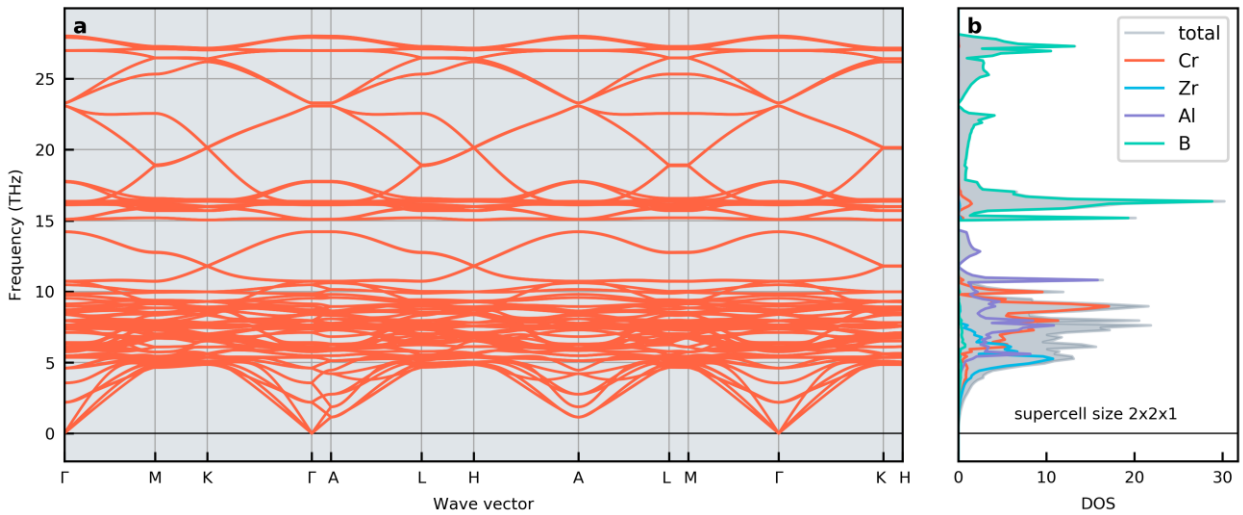

Figure S7. Phonon dispersion and phonon DOS for $Cr_{4/3}Zr_{2/3}AlB_2$ with $R\bar{3}m$ symmetry.

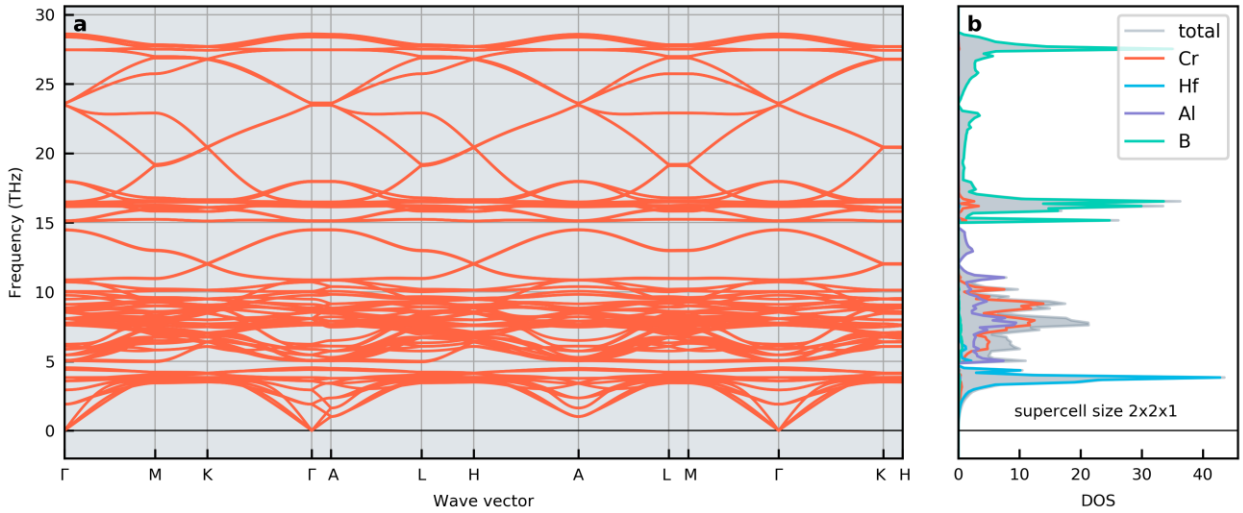

Figure S8. Phonon dispersion and phonon DOS for $Cr_{4/3}Hf_{2/3}AlB_2$ with $R\bar{3}m$ symmetry.

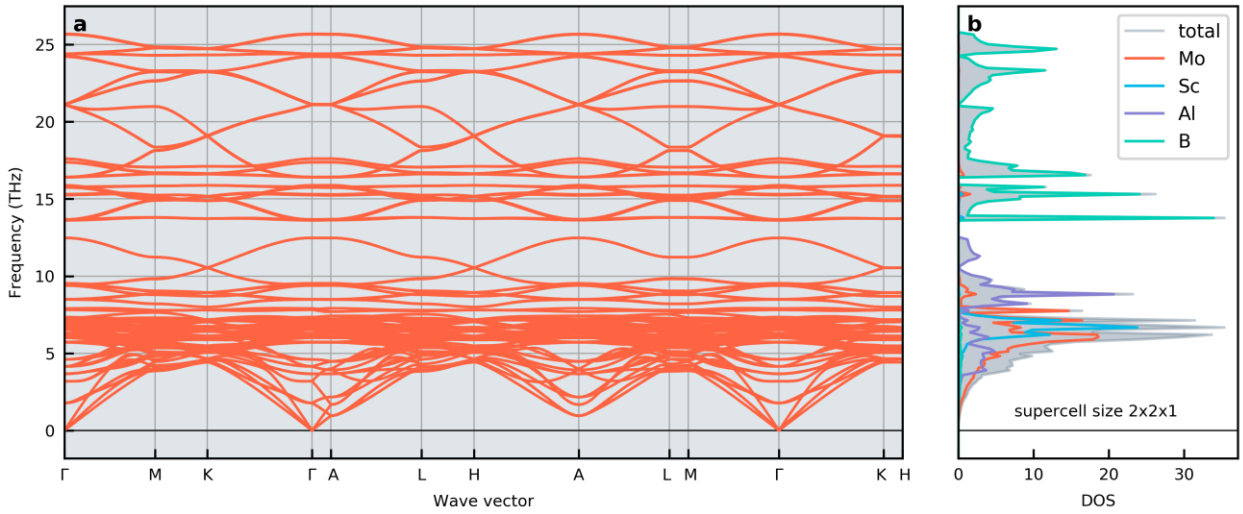

Figure S9. Phonon dispersion and phonon DOS for $Mo_{4/3}Sc_{2/3}AlB_2$ with $R\bar{3}m$ symmetry.

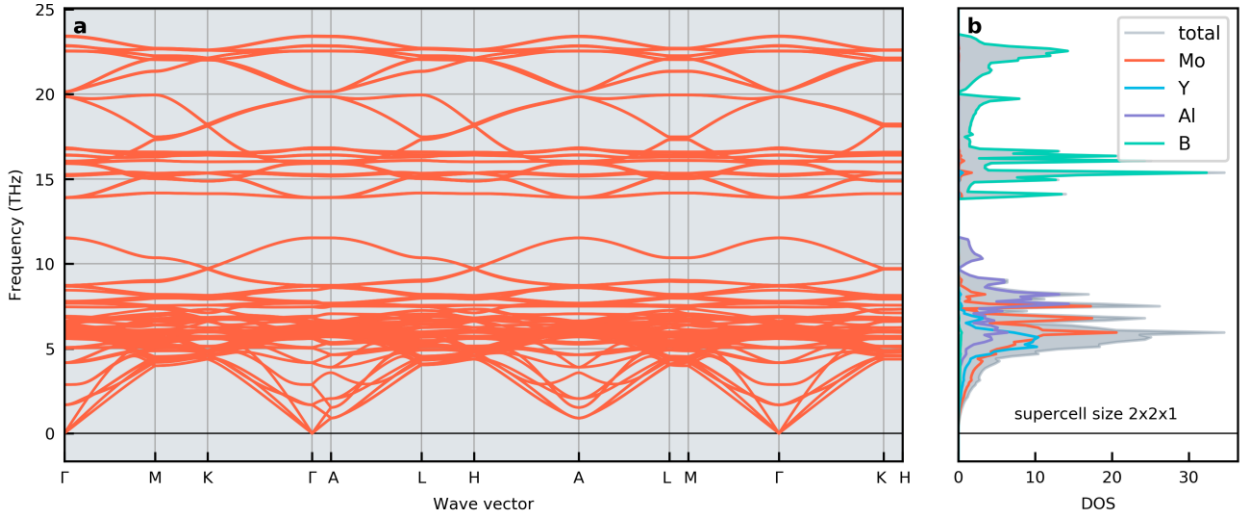

Figure S10. Phonon dispersion and phonon DOS for $Mo_{4/3}Y_{2/3}AlB_2$ with $R\bar{3}m$ symmetry.

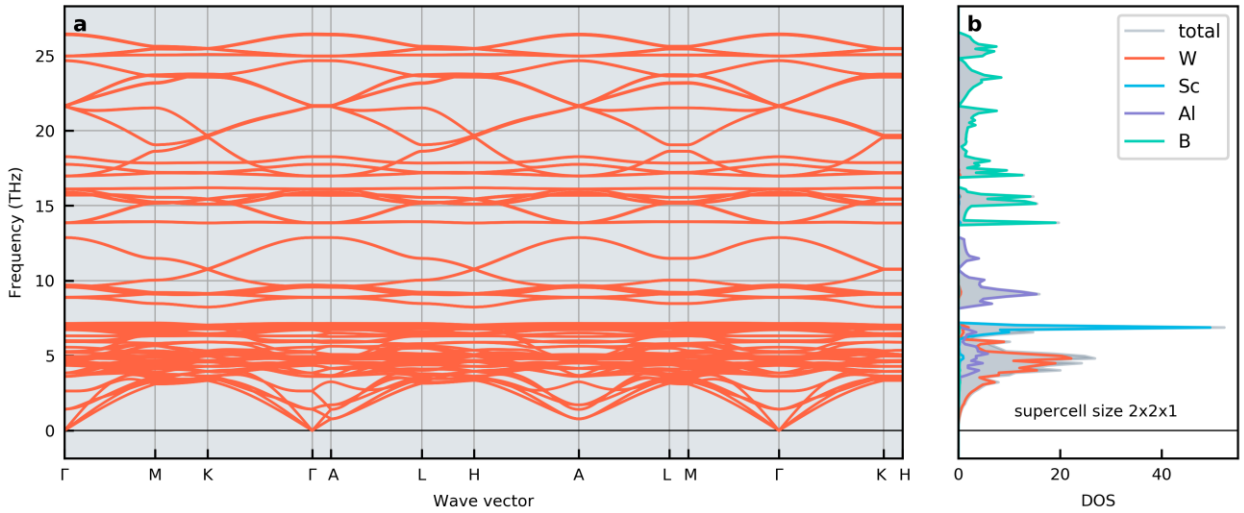

Figure S11. Phonon dispersion and phonon DOS for $W_{4/3}Sc_{2/3}AlB_2$ with $R\bar{3}m$ symmetry.

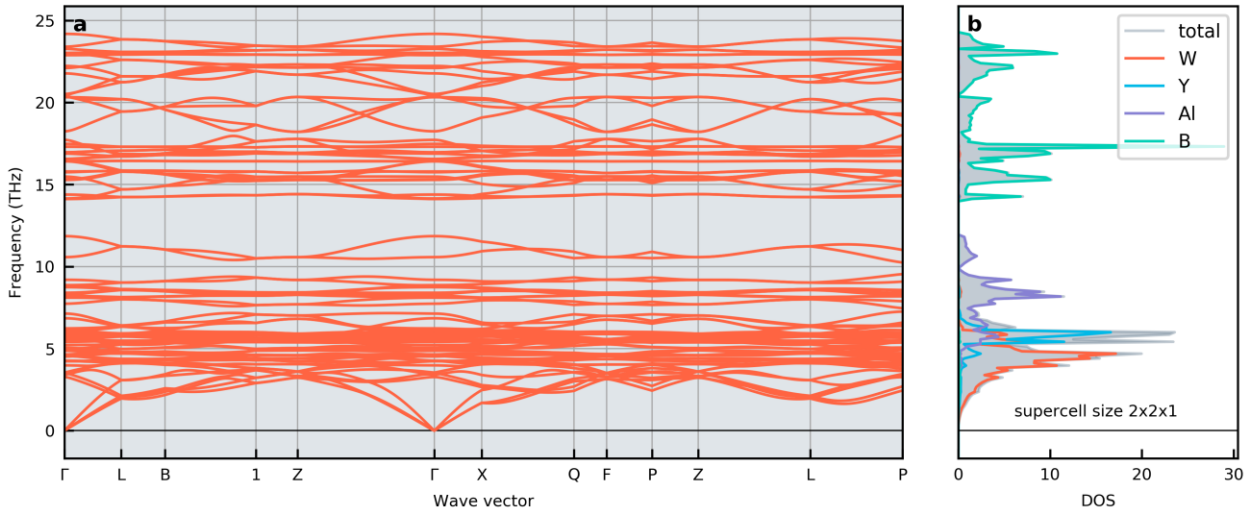

Figure S12. Phonon dispersion and phonon DOS for $W_{4/3}Y_{2/3}AlB_2$ with $C2$ symmetry.

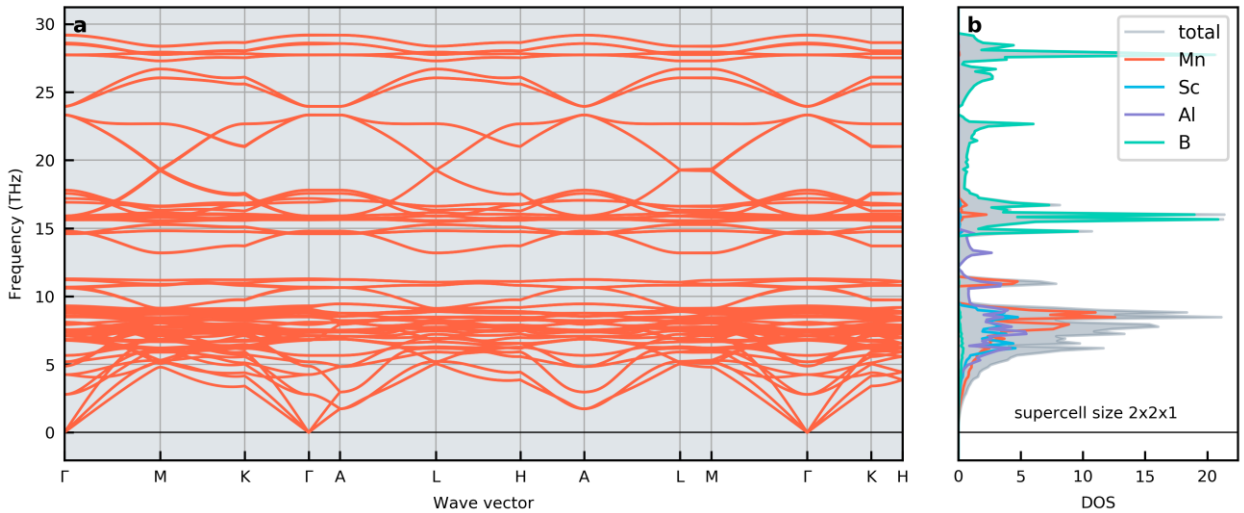

Figure S13. Phonon dispersion and phonon DOS for $Mn_{4/3}Sc_{2/3}AlB_2$ with $P\bar{6}2c$ symmetry.

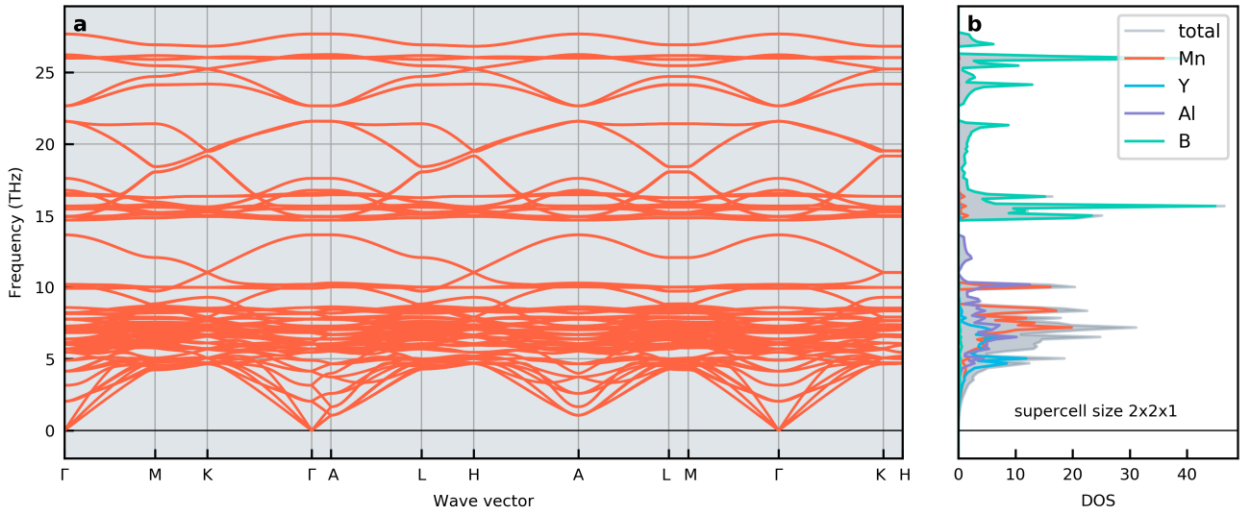

Figure S14. Phonon dispersion and phonon DOS for $Mn_{4/3}Y_{2/3}AlB_2$ with $R\bar{3}m$ symmetry.

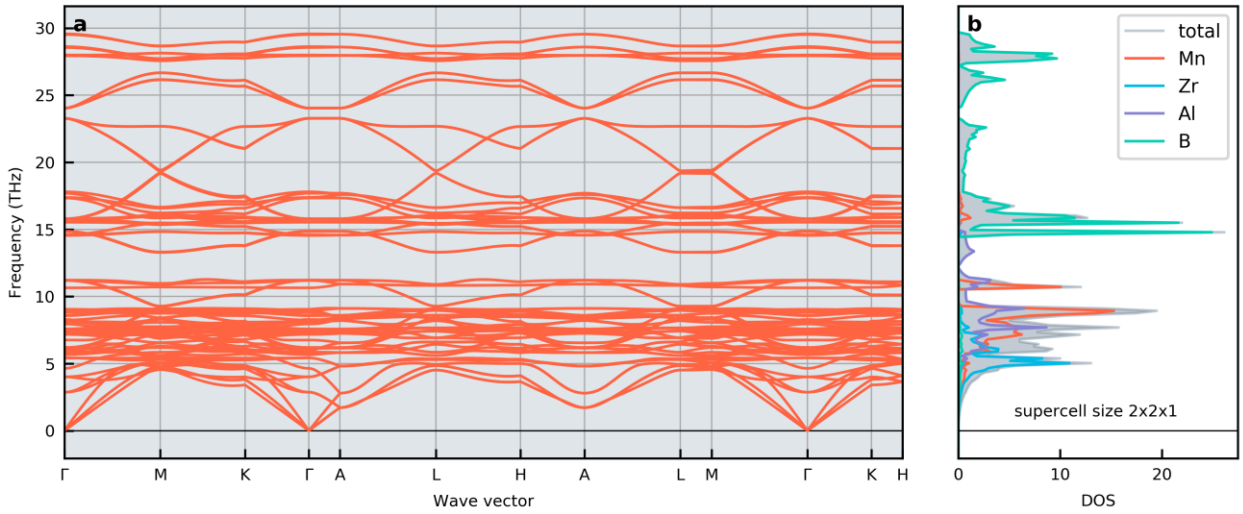

Figure S15. Phonon dispersion and phonon DOS for $Mn_{4/3}Zr_{2/3}AlB_2$ with $P\bar{6}2c$ symmetry.

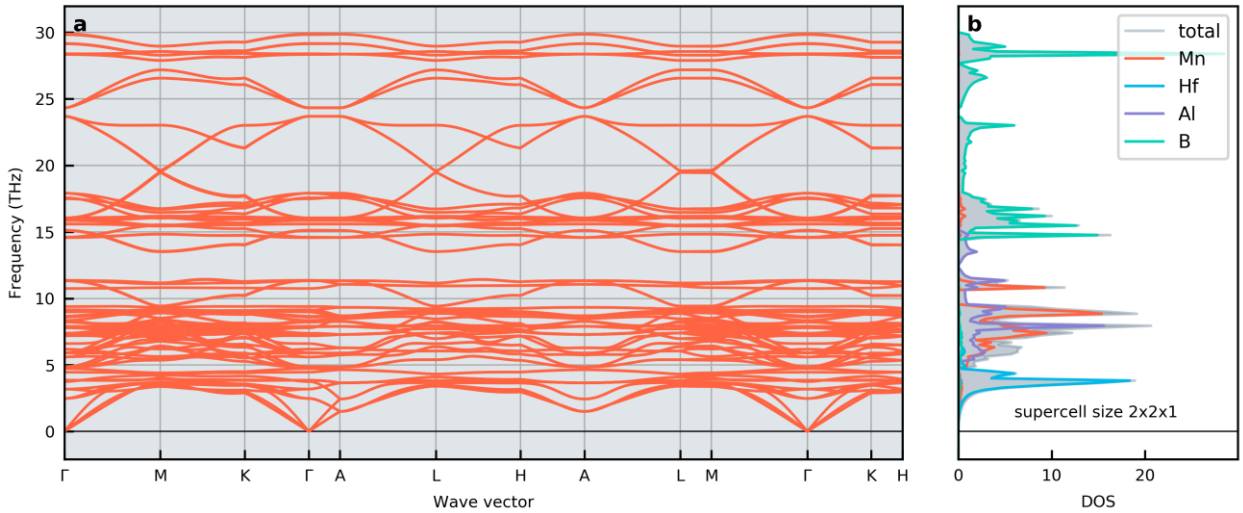

Figure S16. Phonon dispersion and phonon DOS for $Mn_{4/3}Hf_{2/3}AlB_2$ with $P\bar{6}2c$ symmetry.

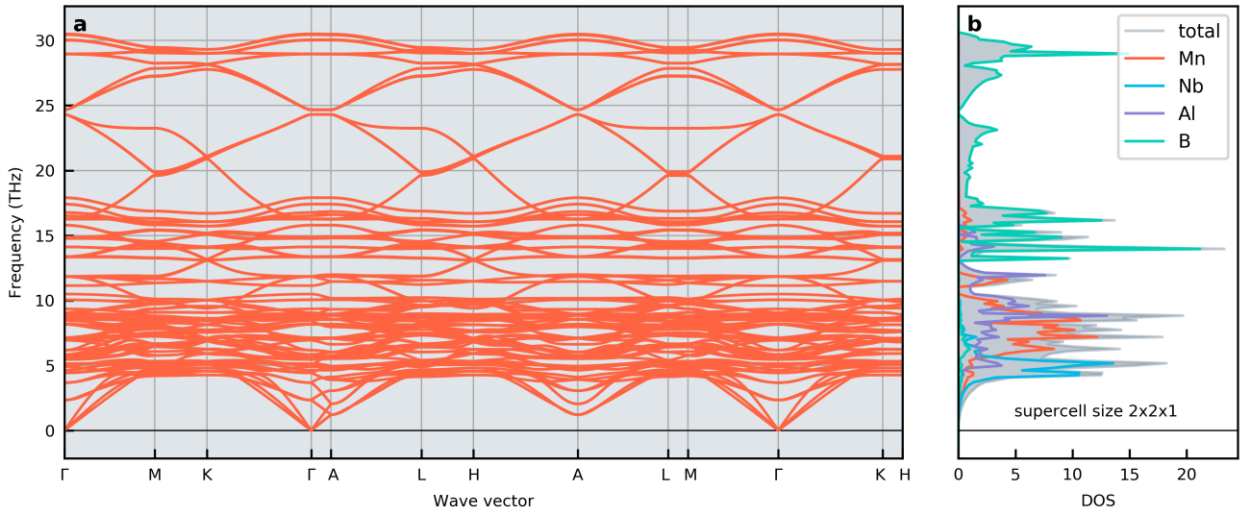

Figure S17. Phonon dispersion and phonon DOS for $Mn_{4/3}Nb_{2/3}AlB_2$ with $R\bar{3}m$ symmetry.

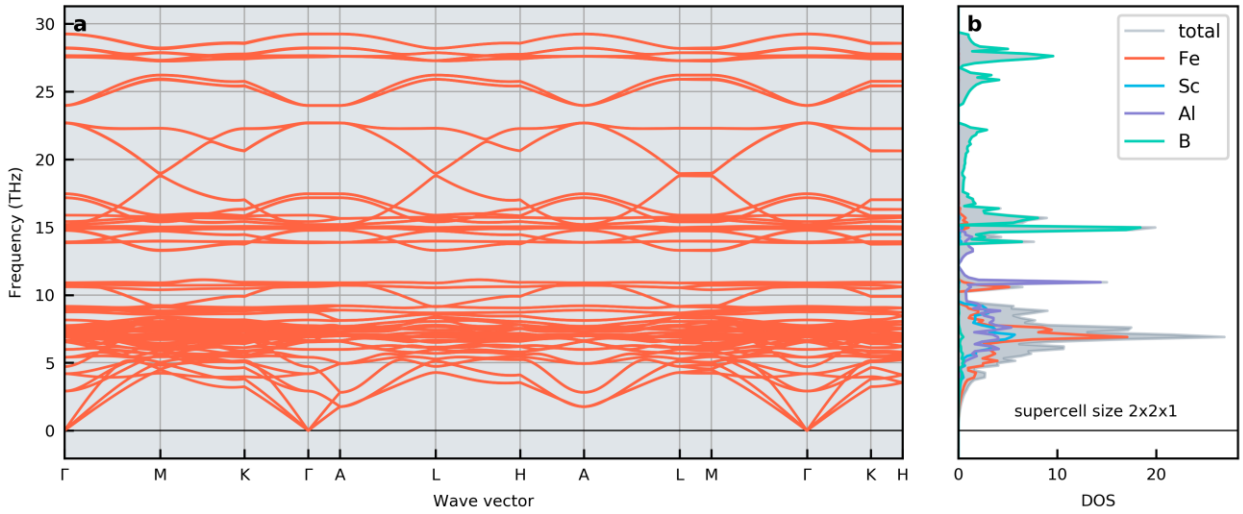

Figure S18. Phonon dispersion and phonon DOS for $Fe_{4/3}Sc_{2/3}AlB_2$ with $P\bar{6}2c$ symmetry.

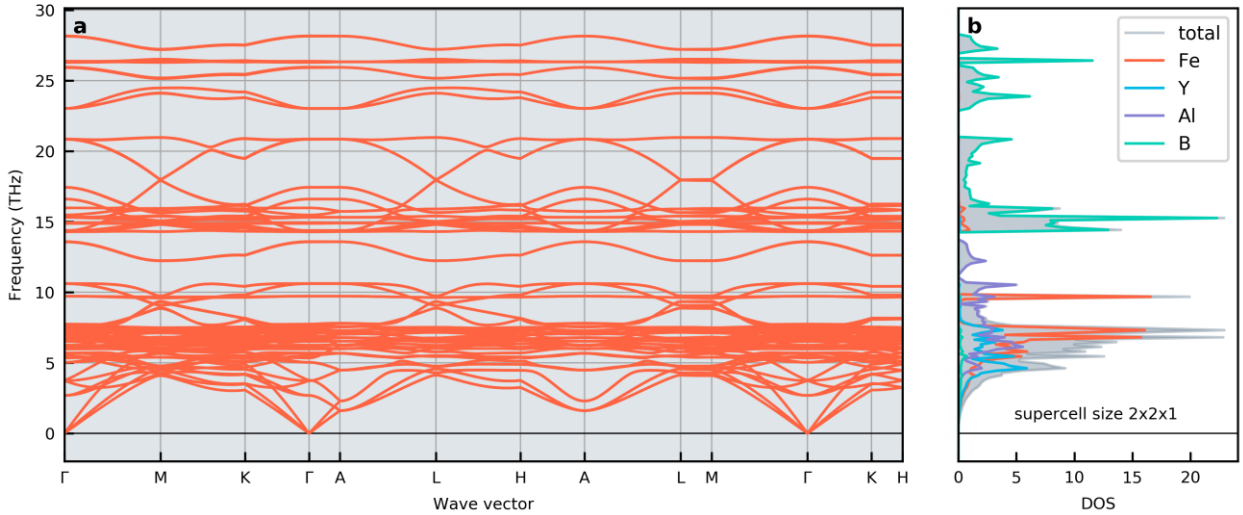

Figure S19. Phonon dispersion and phonon DOS for $Fe_{4/3}Y_{2/3}AlB_2$ with $P\bar{6}2c$ symmetry.

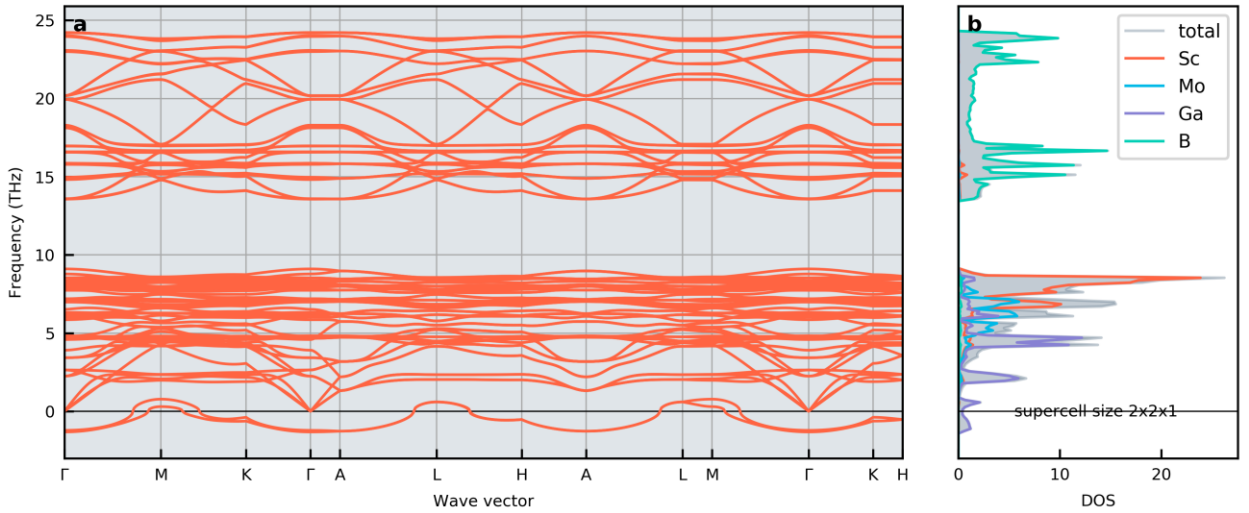

Figure S20. Phonon dispersion and phonon DOS for $Sc_{4/3}Mo_{2/3}GaB_2$ with $P\bar{6}2c$ symmetry.

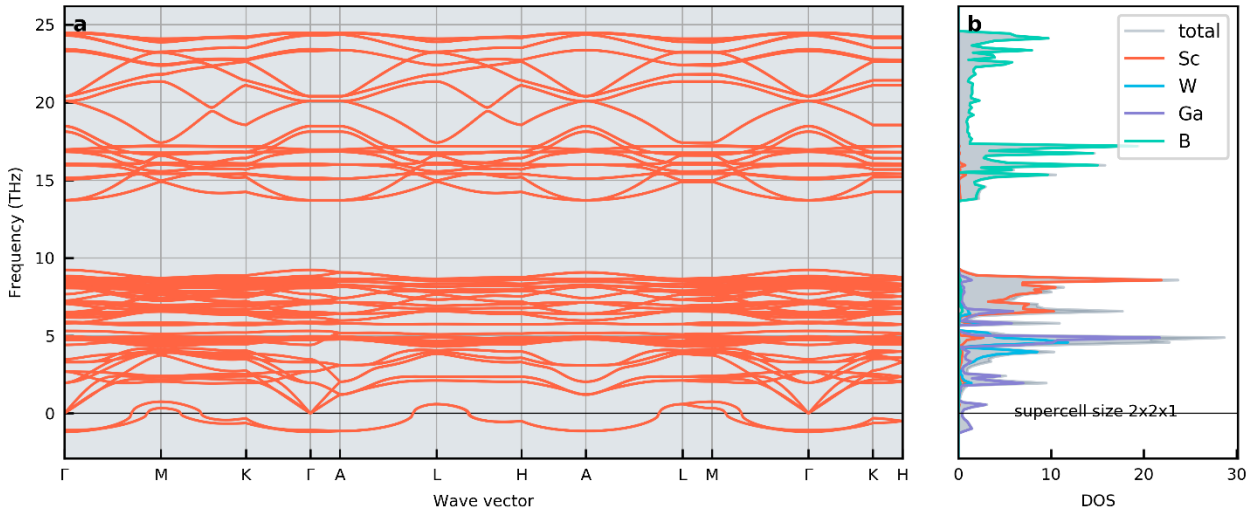

Figure S21. Phonon dispersion and phonon DOS for $Sc_{4/3}W_{2/3}GaB_2$ with $P\bar{6}2c$ symmetry.

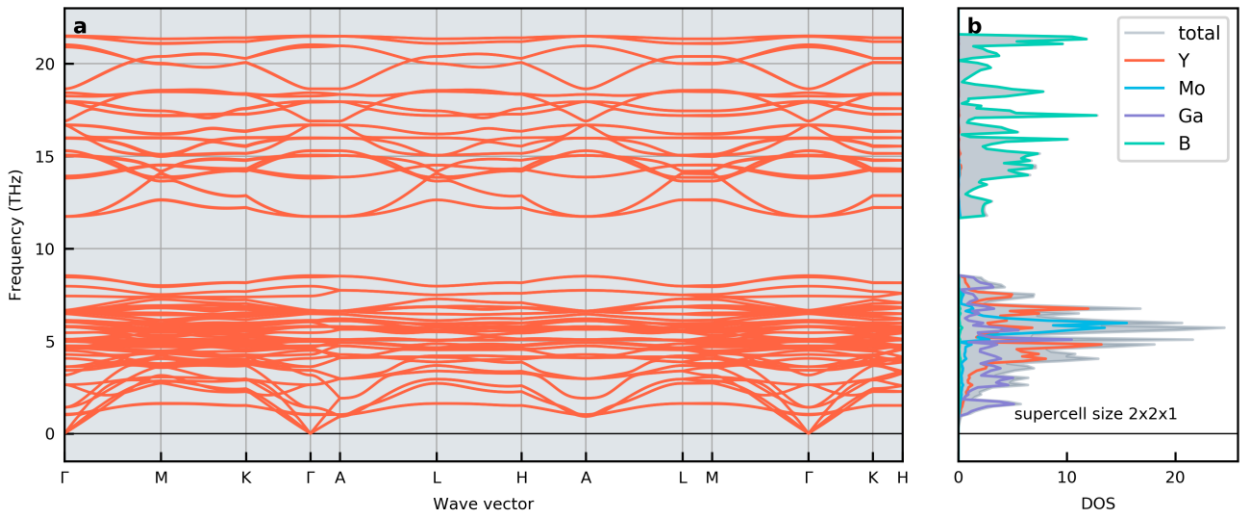

Figure S22. Phonon dispersion and phonon DOS for $Y_{4/3}Mo_{2/3}GaB_2$ with $P\bar{6}2c$ symmetry.

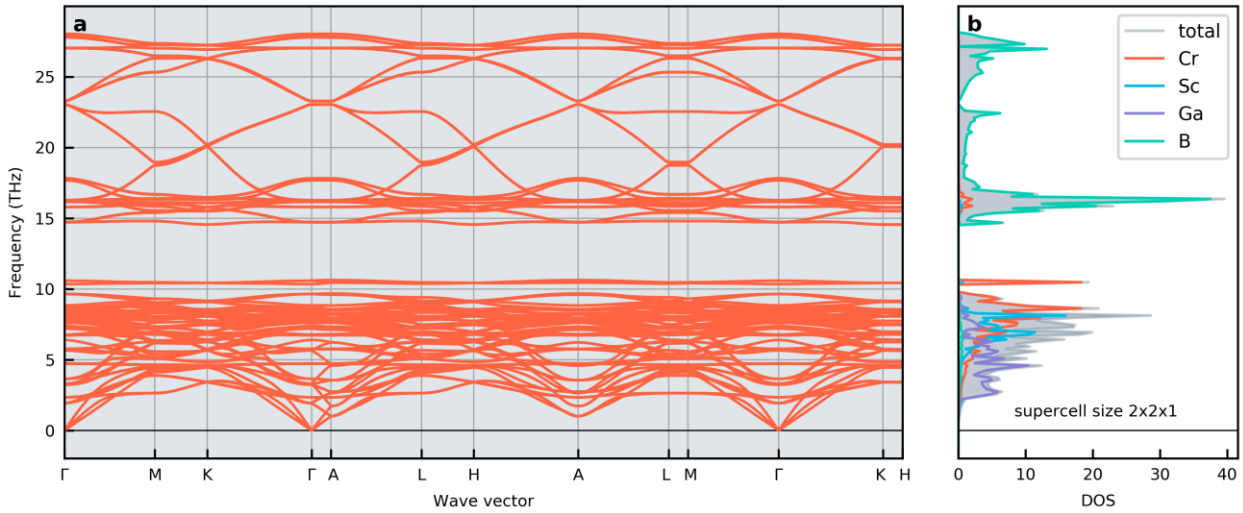

Figure S23. Phonon dispersion and phonon DOS for $Cr_{4/3}Sc_{2/3}GaB_2$ with $R\bar{3}m$ symmetry.

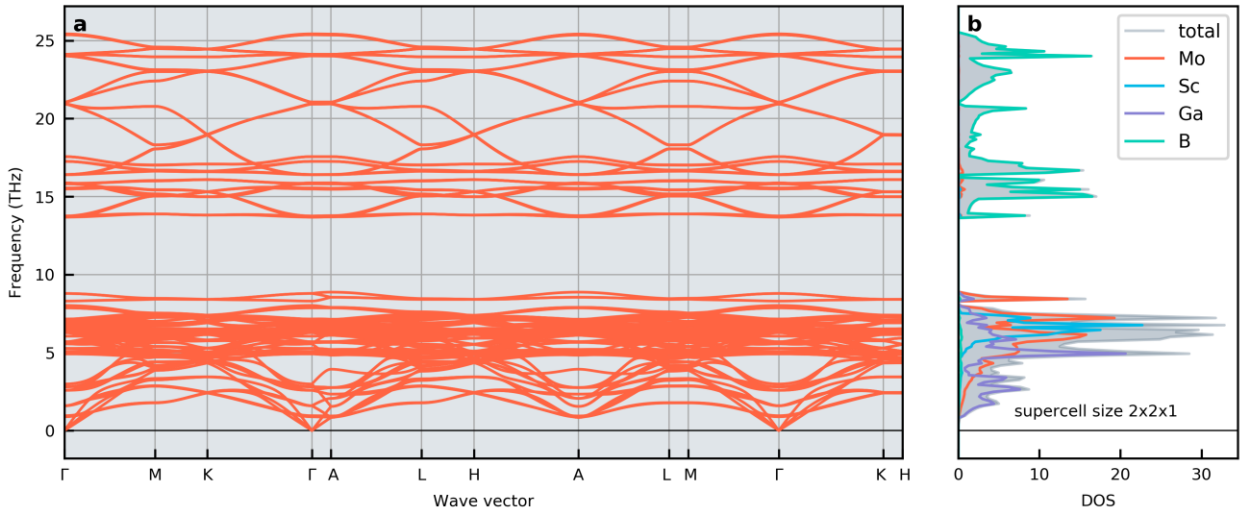

Figure S24. Phonon dispersion and phonon DOS for $Mo_{4/3}Sc_{2/3}GaB_2$ with $R\bar{3}m$ symmetry.

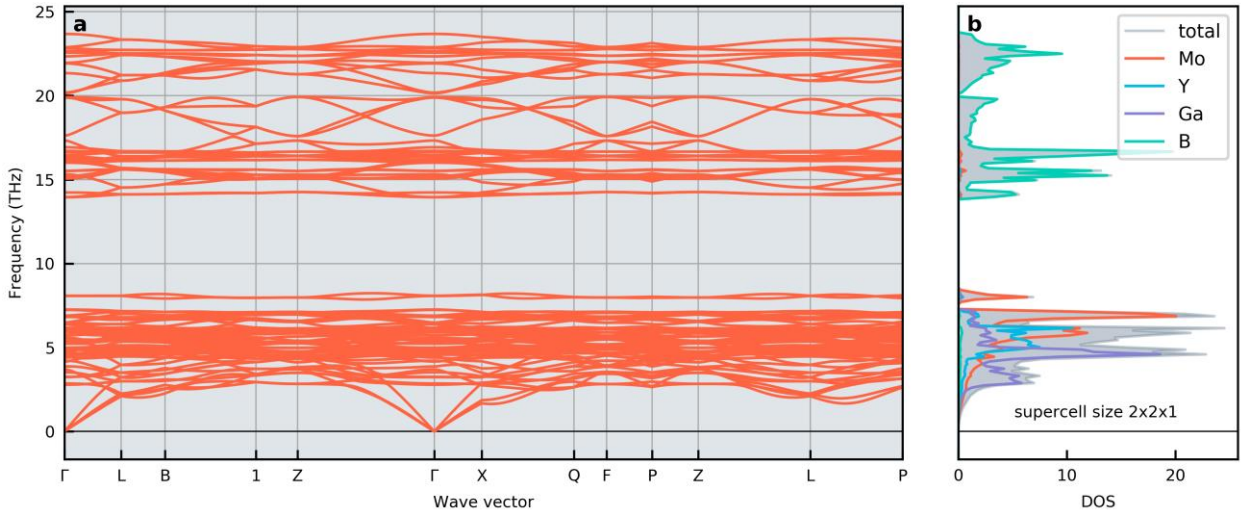

Figure S25. Phonon dispersion and phonon DOS for $Mo_{4/3}Y_{2/3}GaB_2$ with $C2$ symmetry.

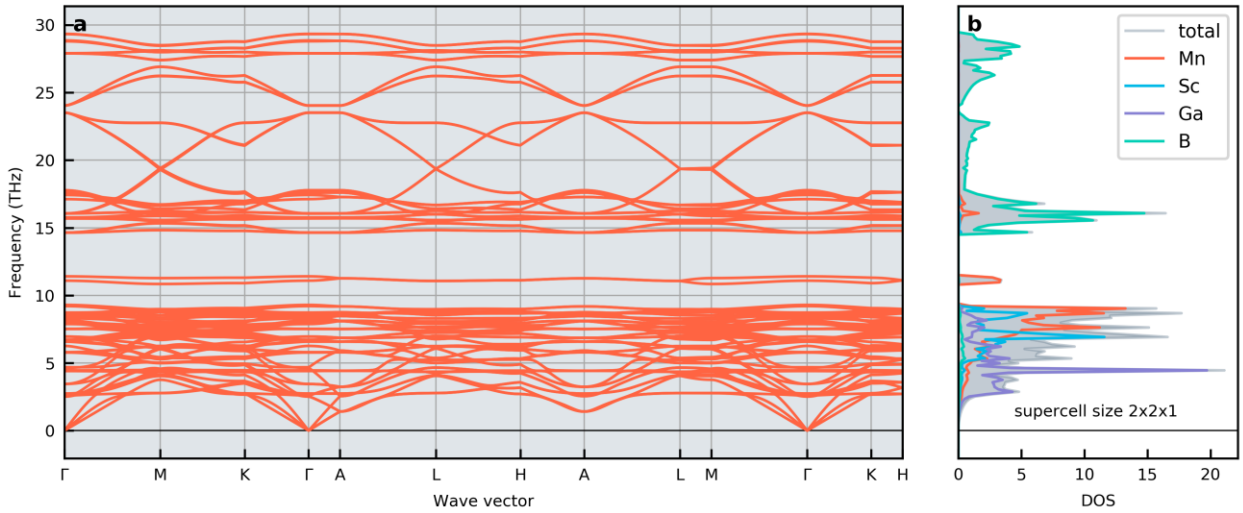

Figure S26. Phonon dispersion and phonon DOS for $Mn_{4/3}Sc_{2/3}GaB_2$ with $P\bar{6}2c$ symmetry

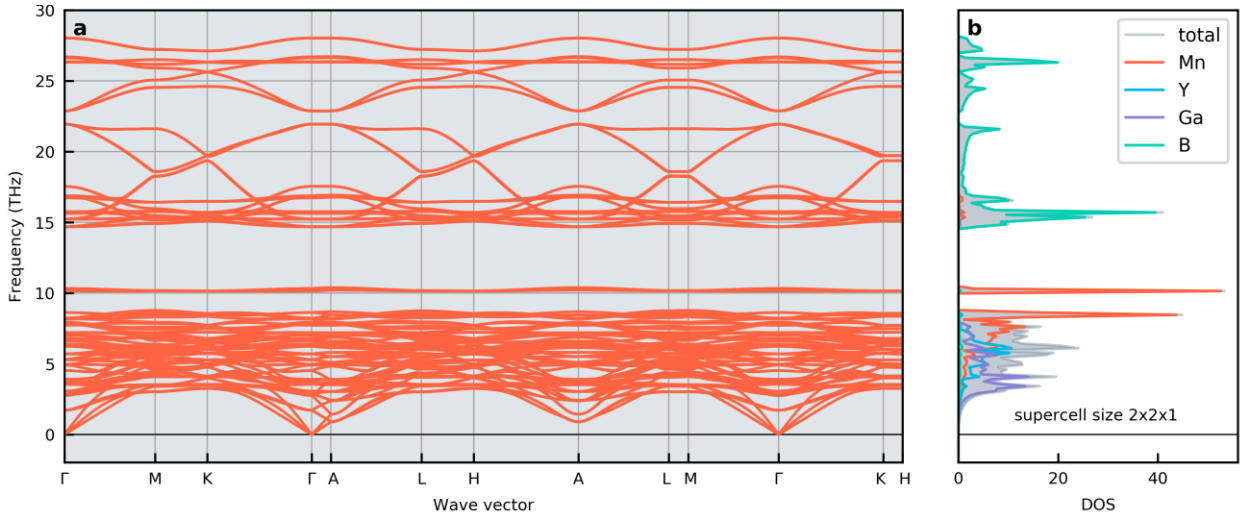

Figure S27. Phonon dispersion and phonon DOS for $Mn_{4/3}Y_{2/3}GaB_2$ with $R\bar{3}m$ symmetry.

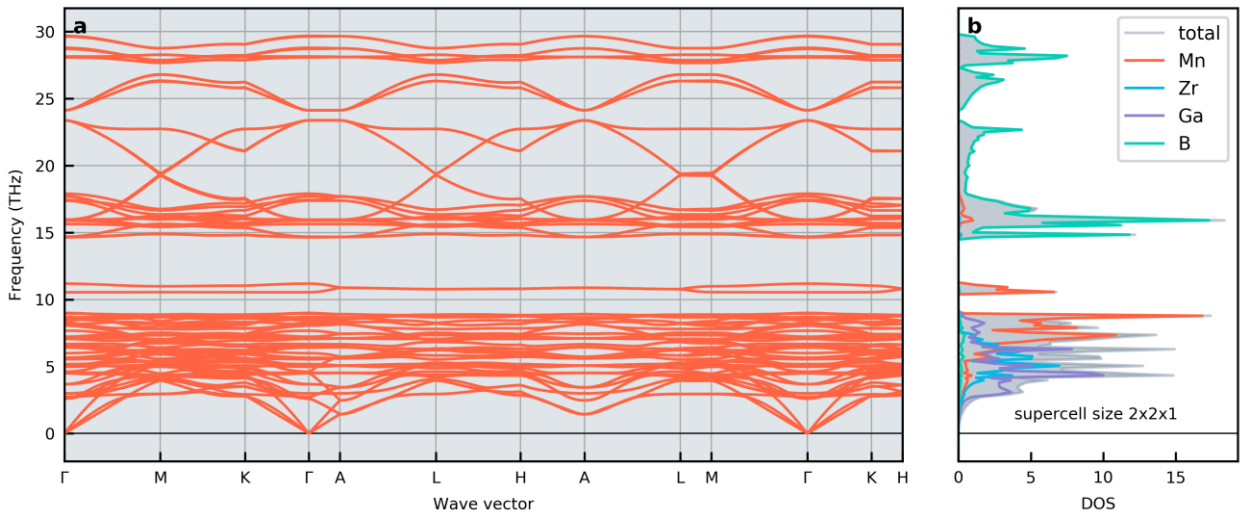

Figure S28. Phonon dispersion and phonon DOS for $Mn_{4/3}Zr_{2/3}GaB_2$ with $P\bar{6}2c$ symmetry

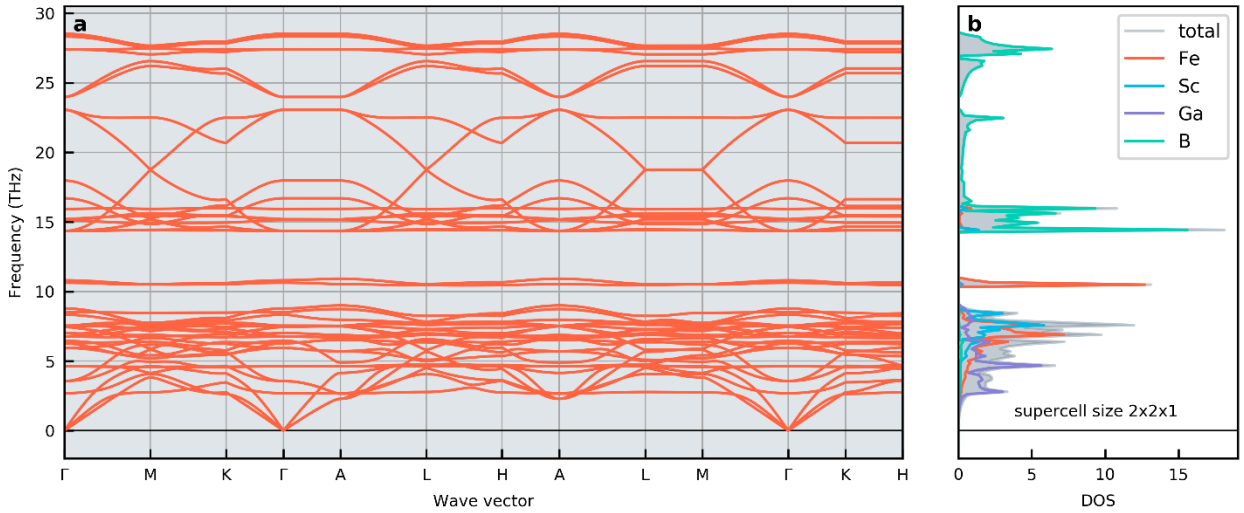

Figure S29. Phonon dispersion and phonon DOS for $Fe_{4/3}Sc_{2/3}GaB_2$ with $P\bar{6}2m$ symmetry

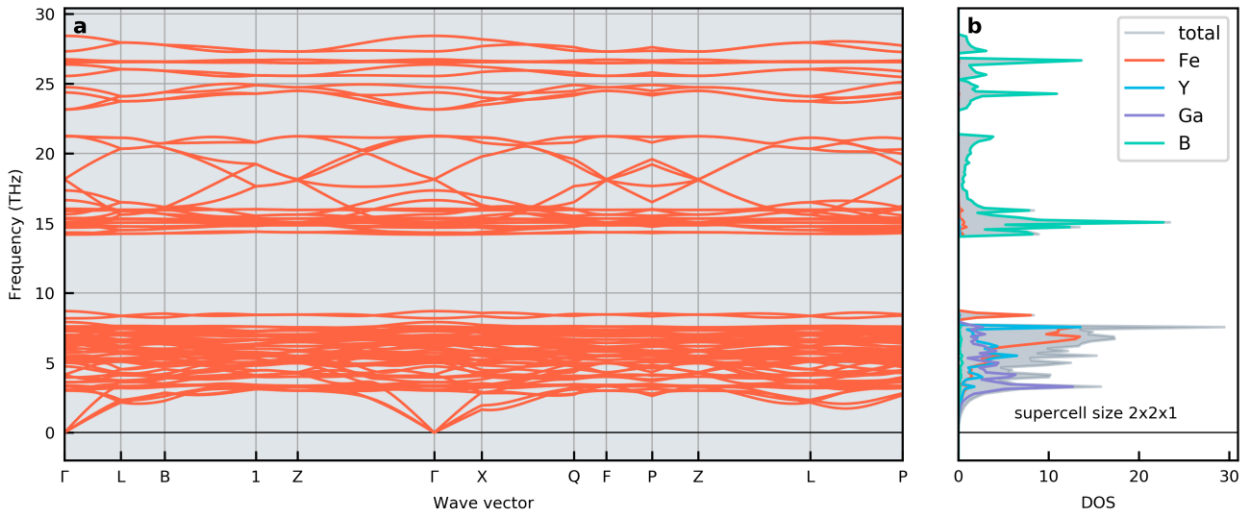

Figure S30. Phonon dispersion and phonon DOS for $Fe_{4/3}Y_{2/3}GaB_2$ with $C2$ symmetry.

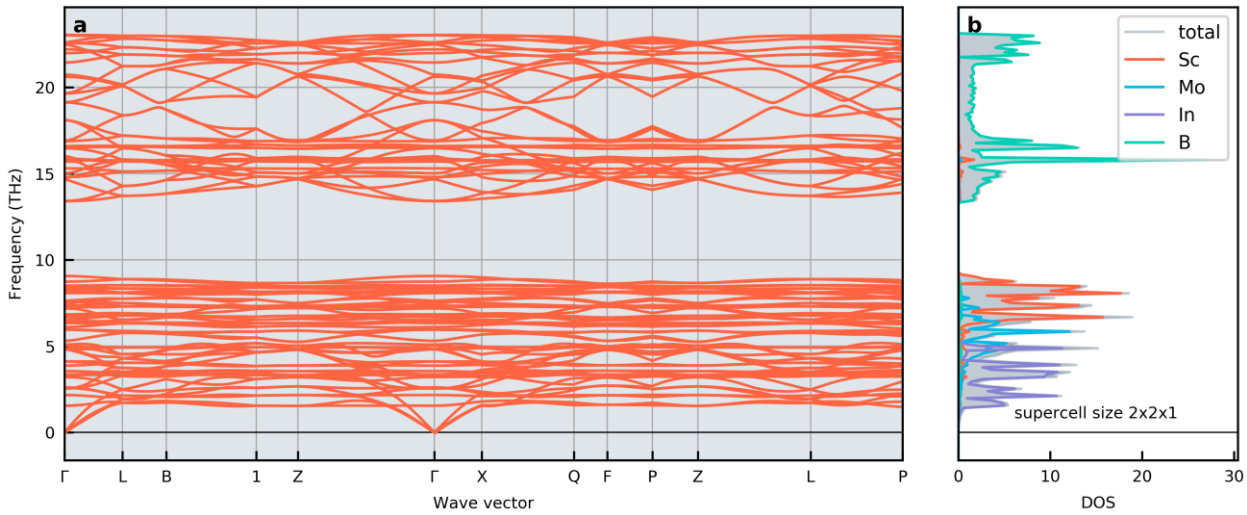

Figure S31. Phonon dispersion and phonon DOS for $Sc_{4/3}Mo_{2/3}InB_2$ with $C2$ symmetry.

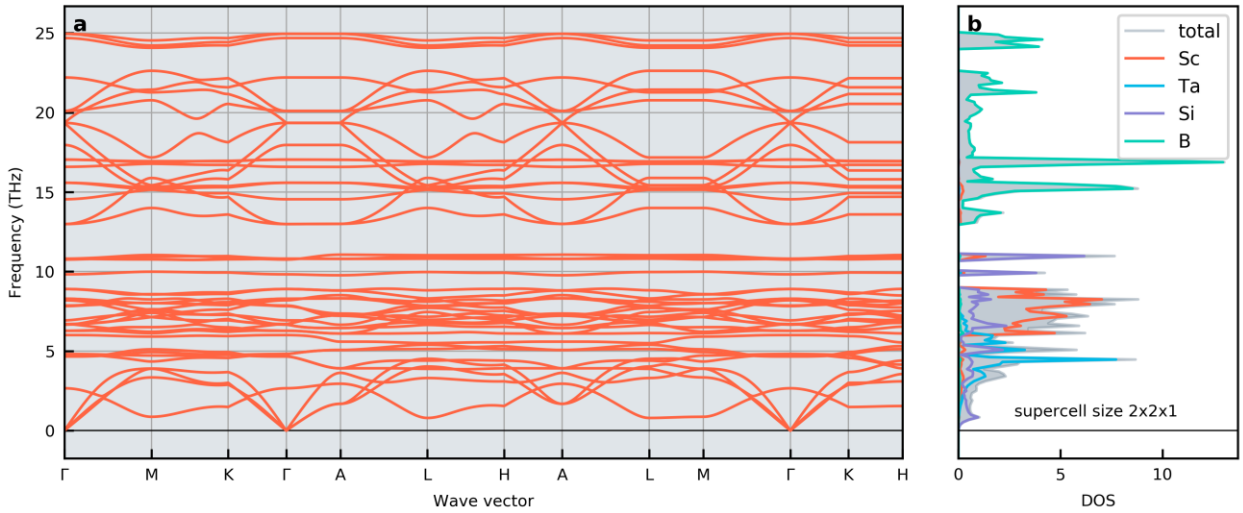

Figure S32. Phonon dispersion and phonon DOS for $Sc_{4/3}Ta_{2/3}SiB_2$ with $P\bar{6}2m$ symmetry.

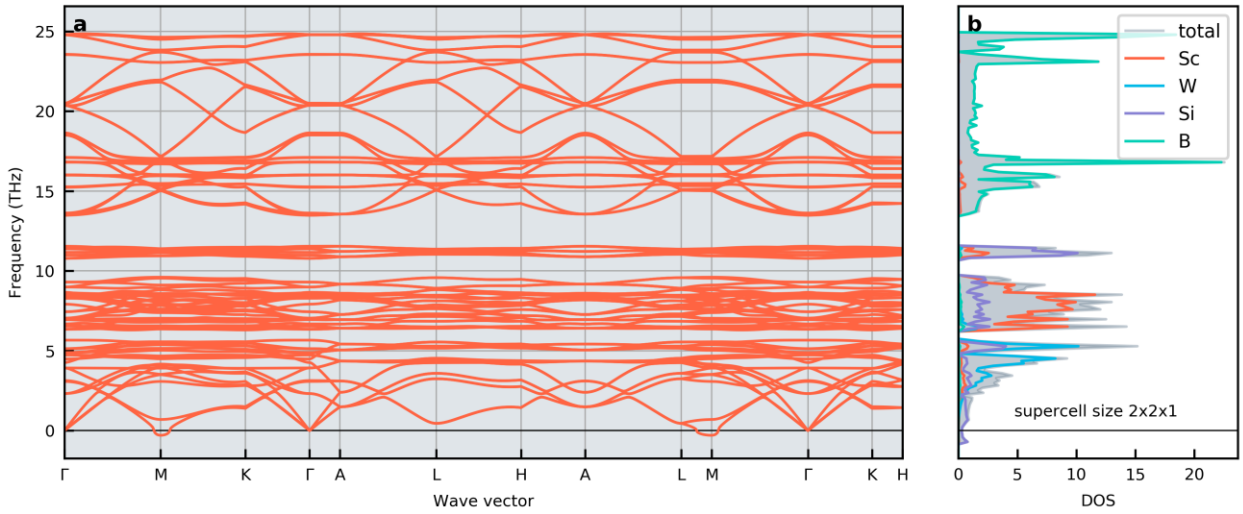

Figure S33. Phonon dispersion and phonon DOS for $Sc_{4/3}W_{2/3}SiB_2$ with $P\bar{6}2c$ symmetry.

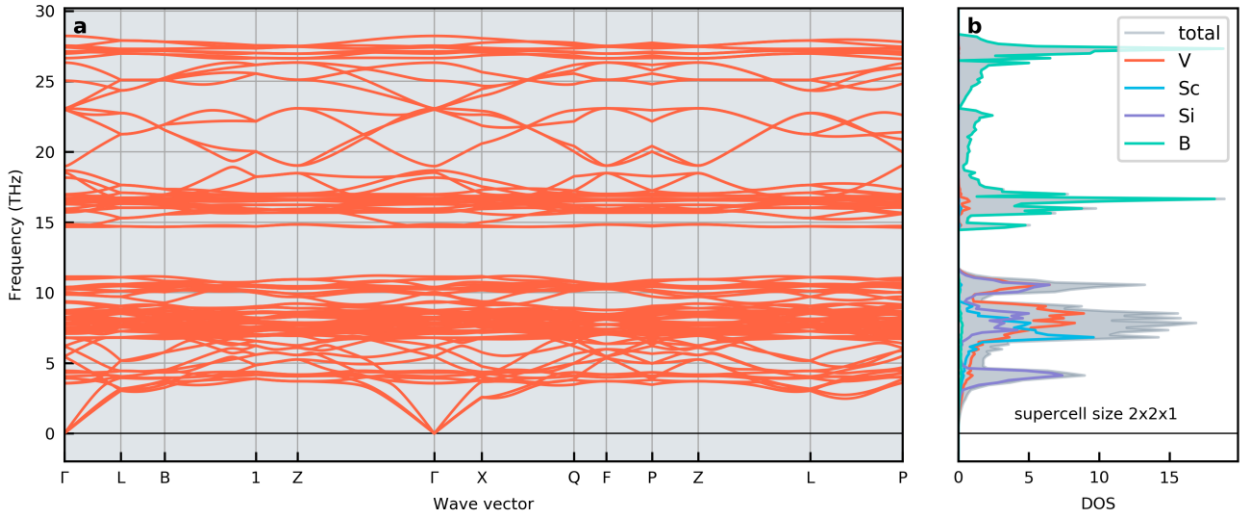

Figure S34. Phonon dispersion and phonon DOS for $V_{4/3}Sc_{2/3}SiB_2$ with $C2$ symmetry.

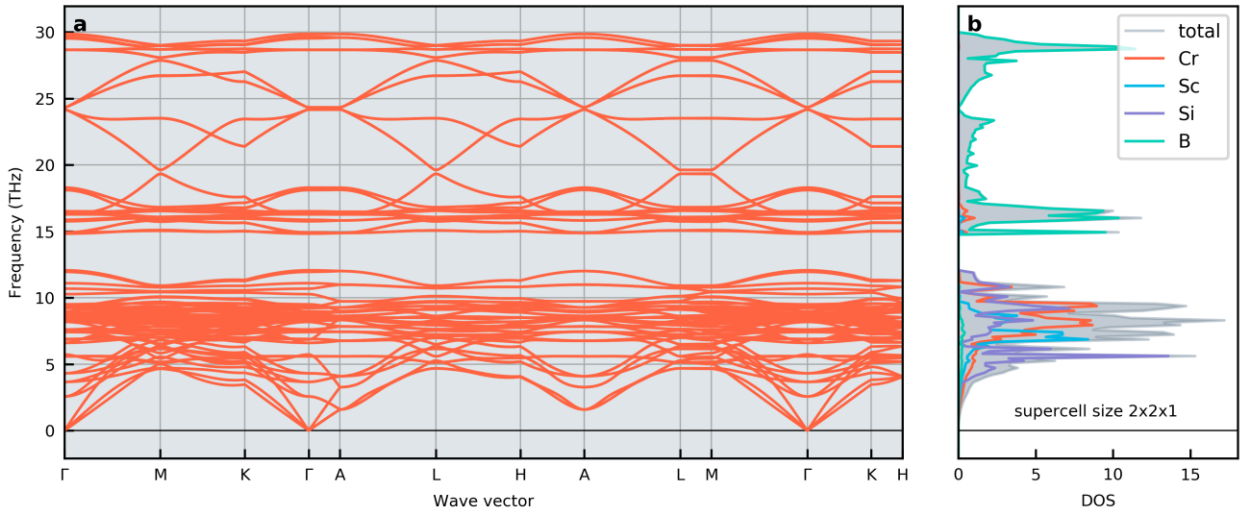

Figure S35. Phonon dispersion and phonon DOS for $Cr_{4/3}Sc_{2/3}SiB_2$ with $P\bar{6}2c$ symmetry.

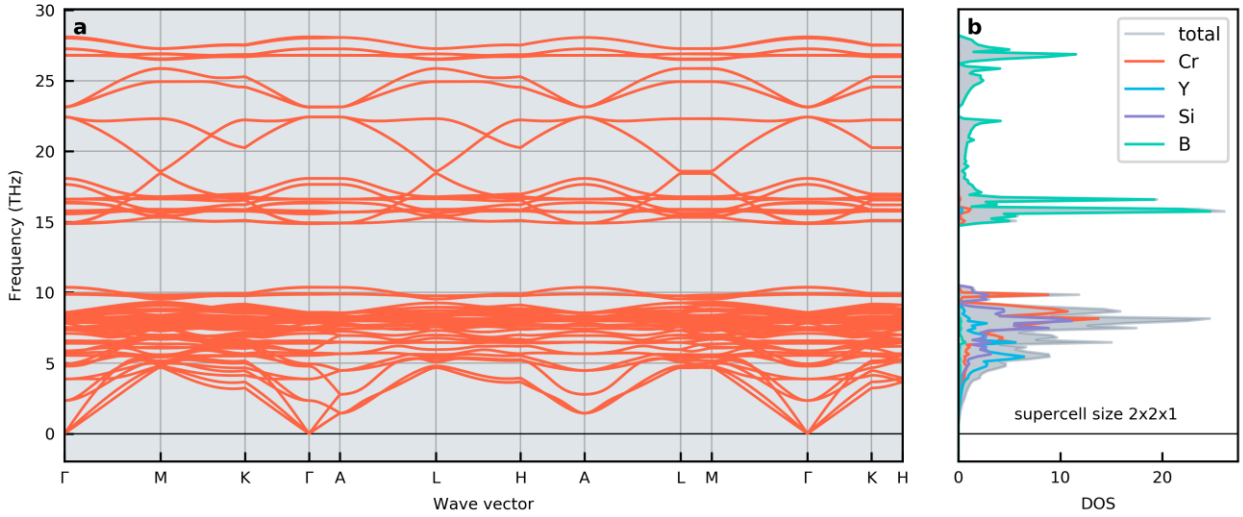

Figure S36. Phonon dispersion and phonon DOS for $Cr_{4/3}Y_{2/3}SiB_2$ with $P\bar{6}2c$ symmetry.

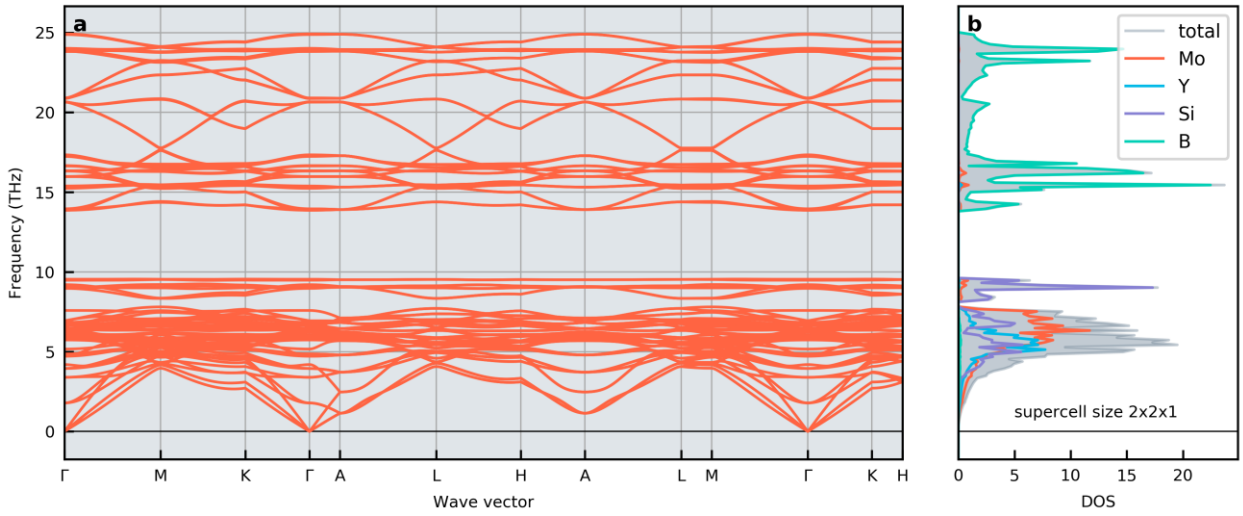

Figure S37. Phonon dispersion and phonon DOS for $Mo_{4/3}Y_{2/3}SiB_2$ with $P\bar{6}2c$ symmetry.

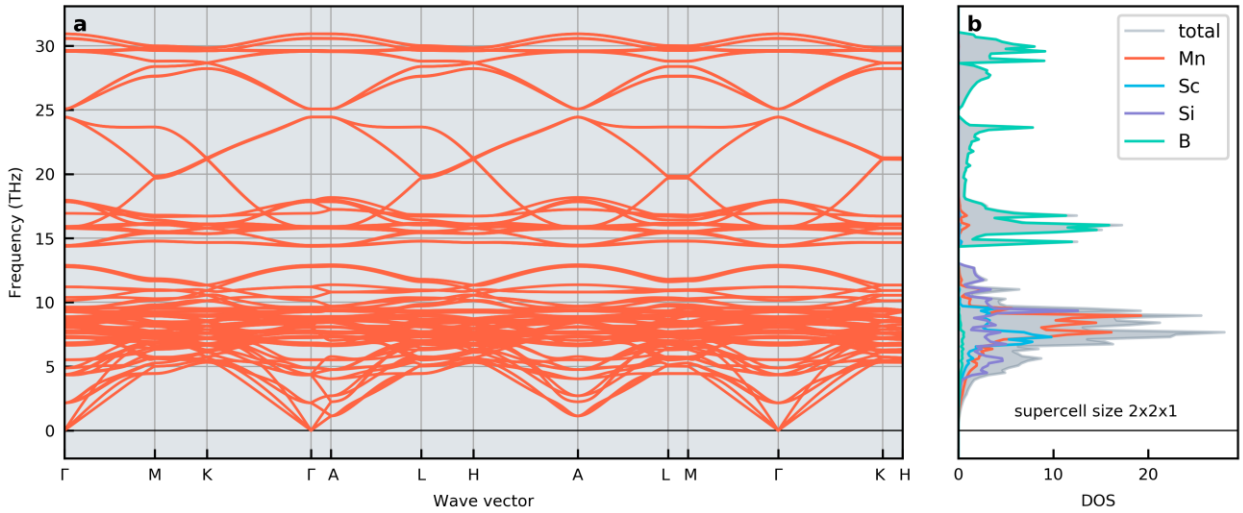

Figure S38. Phonon dispersion and phonon DOS for $Mn_{4/3}Sc_{2/3}SiB_2$ with $R\bar{3}m$ symmetry.

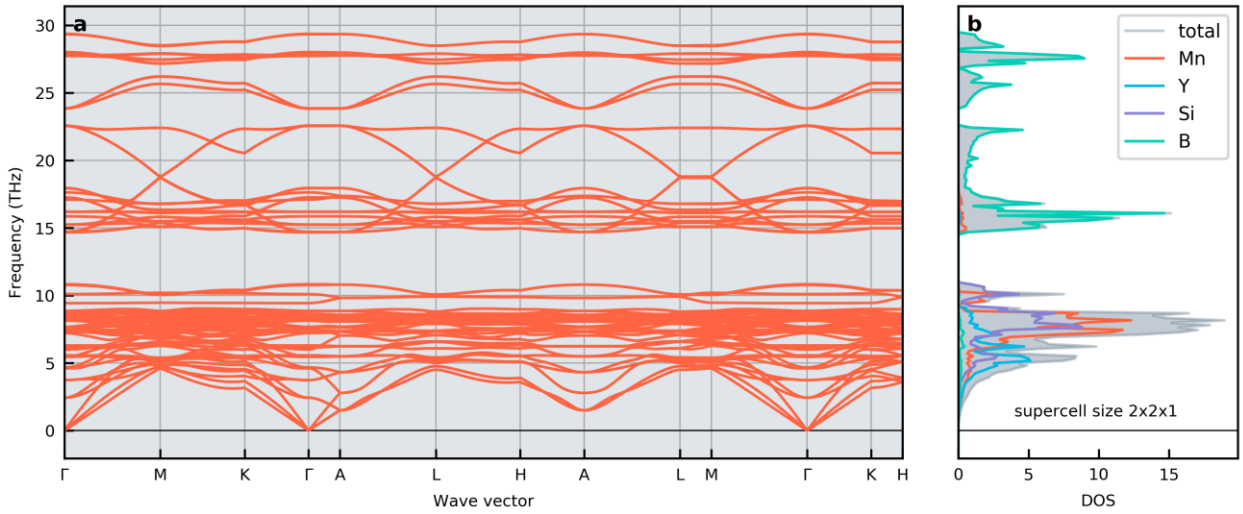

Figure S39. Phonon dispersion and phonon DOS for $Mn_{4/3}Y_{2/3}SiB_2$ with $P\bar{6}2c$ symmetry.

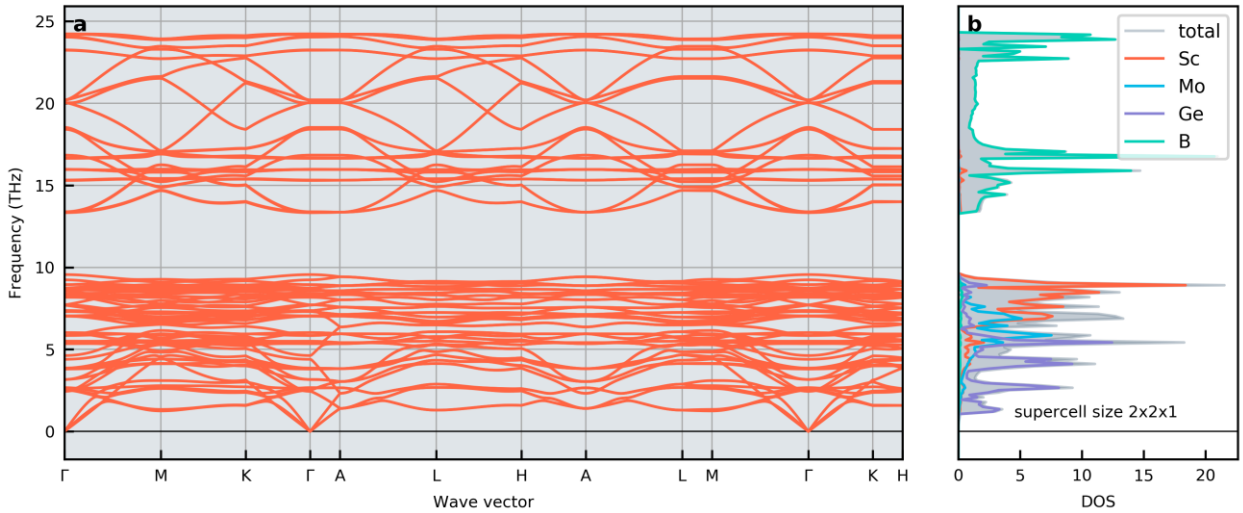

Figure S40. Phonon dispersion and phonon DOS for $Sc_{4/3}Mo_{2/3}GeB_2$ with $P\bar{6}2c$ symmetry.

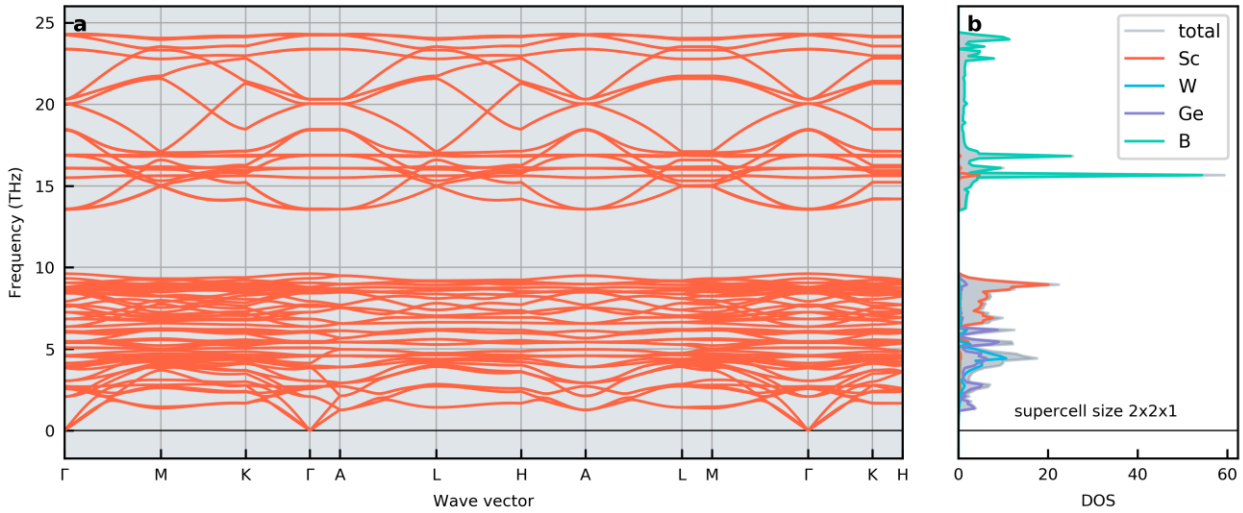

Figure S41. Phonon dispersion and phonon DOS for $Sc_{4/3}W_{2/3}GeB_2$ with $P\bar{6}2c$ symmetry.

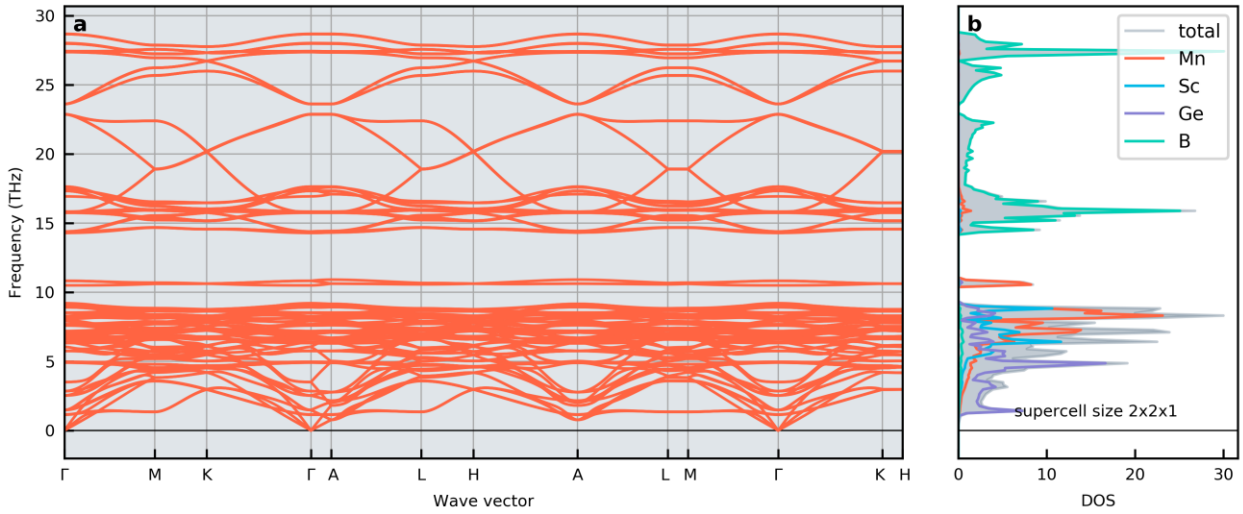

Figure S42. Phonon dispersion and phonon DOS for $Mn_{4/3}Sc_{2/3}GeB_2$ with $R\bar{3}m$ symmetry.

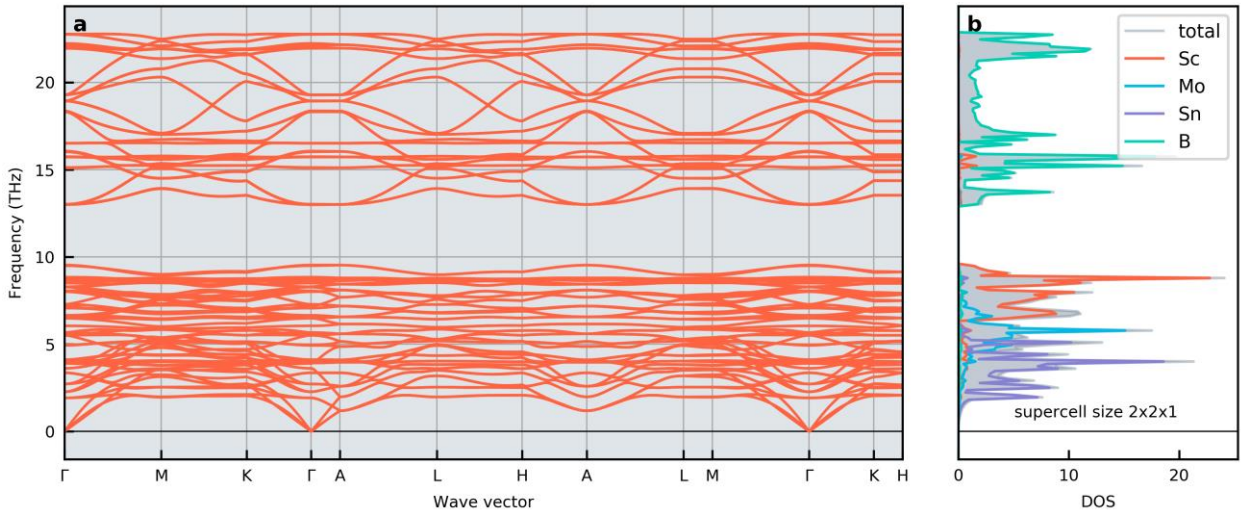

Figure S43. Phonon dispersion and phonon DOS for $Sc_{4/3}Mo_{2/3}SnB_2$ with $P\bar{6}2c$ symmetry.

Table S7. Atomic radius and electronegativity considered for *M* and *A*.[11, 12]

M	Atomic radius r_M (Å)	Electronegativity ρ_M (Pauling scale)	*A*	Atomic radius r_A (Å)	Electronegativity ρ_A (Pauling scale)
Sc	1.62	1.36	Al	1.43	1.61
Y	1.80	1.22	Ga	1.40	1.81
Ti	1.47	1.54	In	1.58	1.78
Zr	1.60	1.33	Si	1.38	1.90
Hf	1.59	1.30	Ge	1.44	2.01
V	1.35	1.63	Sn	1.63	1.96
Nb	1.46	1.60			
Ta	1.46	1.50			
Cr	1.29	1.66			
Mo	1.39	2.16			
W	1.39	2.36			
Mn	1.27	1.55			
Fe	1.26	1.83			
Co	1.25	1.88			

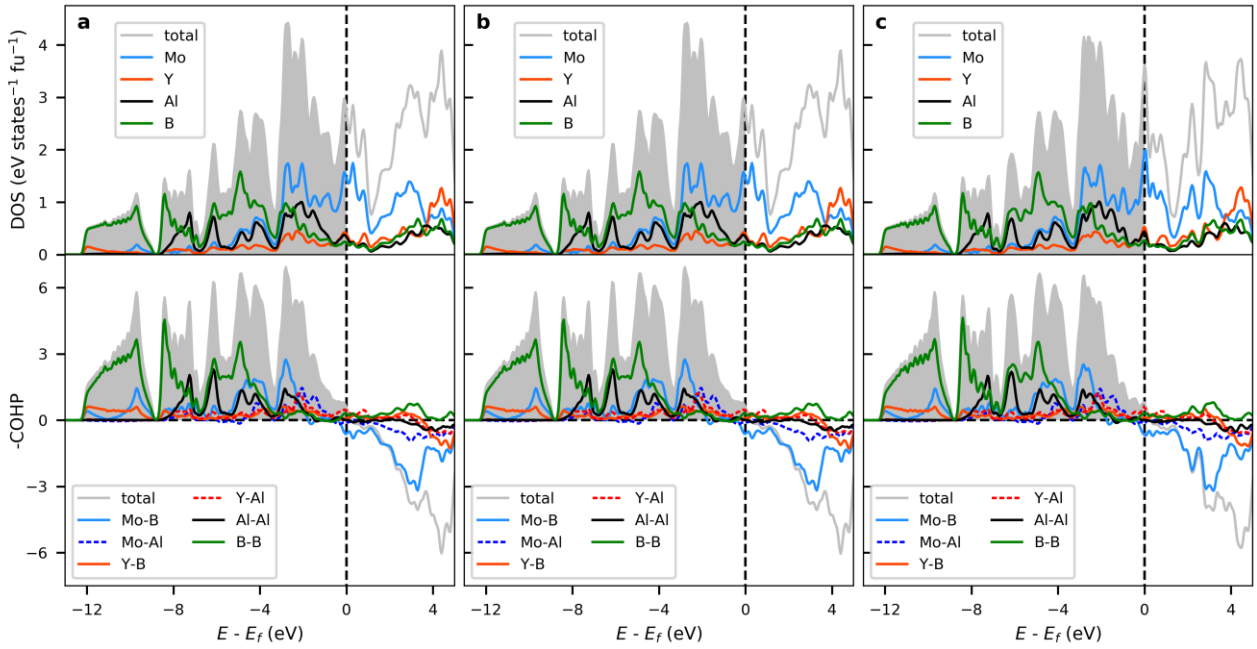

Figure S44. Calculated density of states, DOS, and crystal overlap Hamilton population, COHP, for *i*-MAB phase $Mo_{4/3}Y_{2/3}AlB_2$ in (a) $C2$, (b) $R\bar{3}m$, and (c) $P\bar{6}2c$ space group symmetry. The filled regions represent occupied states, and the Fermi level is set to 0 eV.

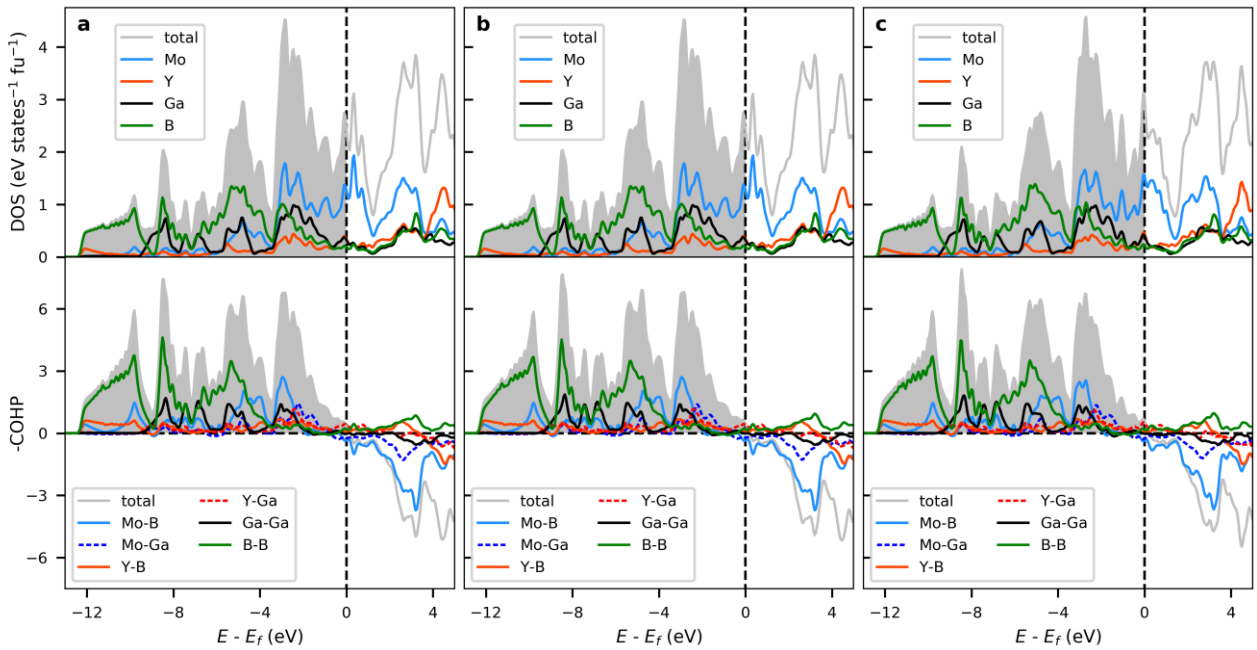

Figure S45. Calculated density of states, DOS, and crystal overlap Hamilton population, COHP, for *i*-MAB phase $Mo_{4/3}Y_{2/3}GaB_2$ in (a) $C2$, (b) $R\bar{3}m$, and (c) $P\bar{6}2c$ space group symmetry. The filled regions represent occupied states, and the Fermi level is set to 0 eV.

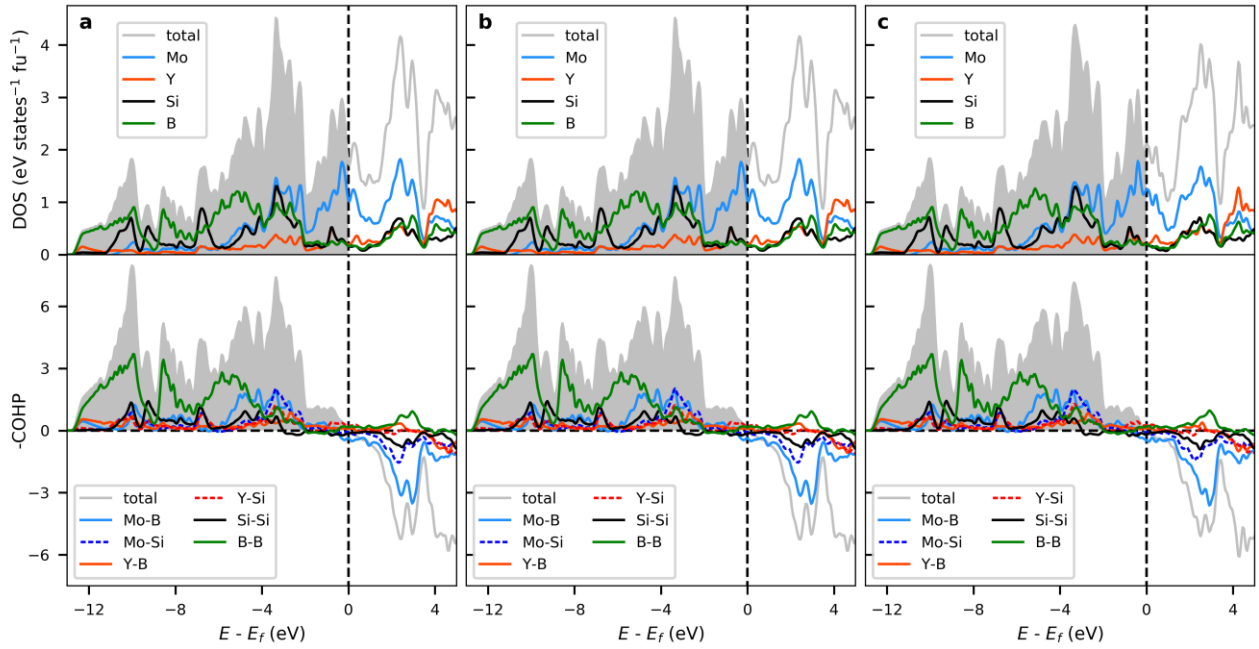

Figure S46. Calculated density of states, DOS, and crystal overlap Hamilton population, COHP, for *i*-MAB phase $Mo_{4/3}Y_{2/3}SiB_2$ in (a) $C2$, (b) $R\bar{3}m$, and (c) $P\bar{6}2c$ space group symmetry. The filled regions represent occupied states, and the Fermi level is set to 0 eV.

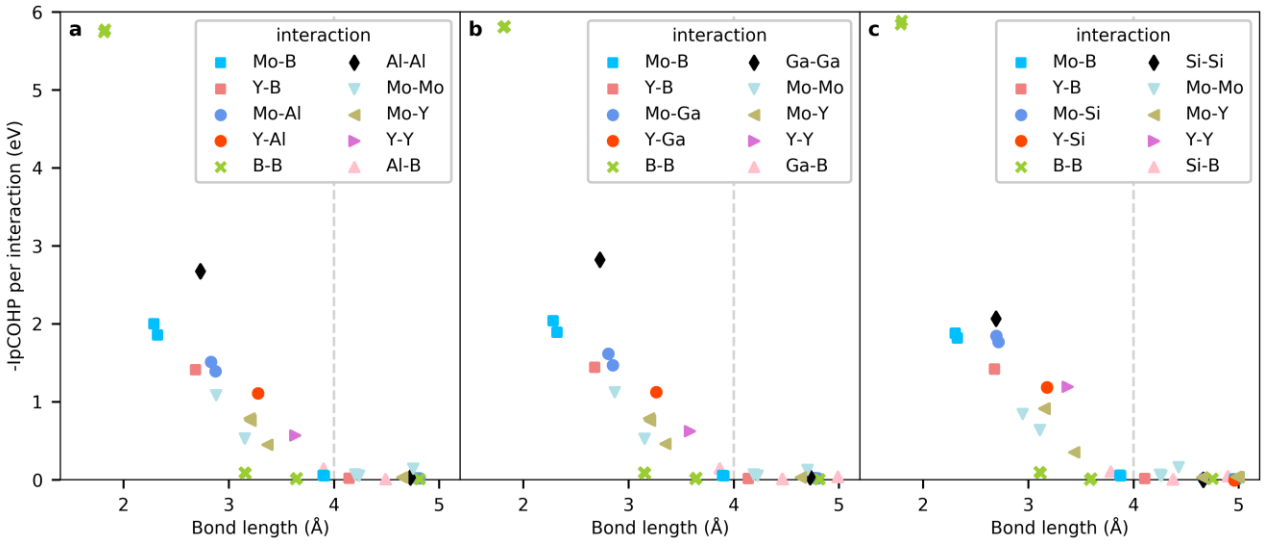

Figure S47. Integrated crystal overlap Hamilton population, IpCOHP, for individual interactions in *i*-MAB phase $Mo_{4/3}Y_{2/3}AB_2$ with $R\bar{3}m$ space group symmetry for (a) A = Al, (b) A = Ga, and (c) A = Si. IpCOHP obtained for all interactions up to 5 Å.

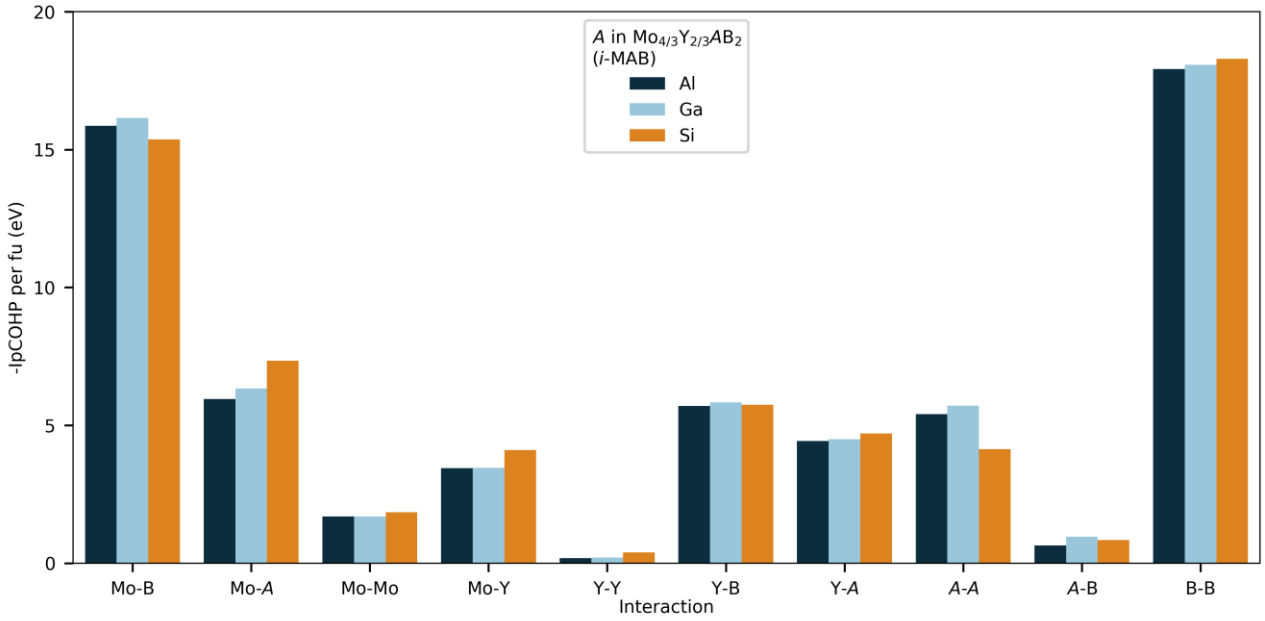

Figure S48. Comparison of bonding strength in selected *i*-MAB phases. Total integrated crystal overlap Hamilton population, IpCOHP, per formula unit of *i*-MAB phase $Mo_{4/3}Y_{2/3}AB_2$ with $R\bar{3}m$ space group symmetry for *A* = Al, Ga, Si. Values obtained by summing up each type of interaction up to 5 Å.

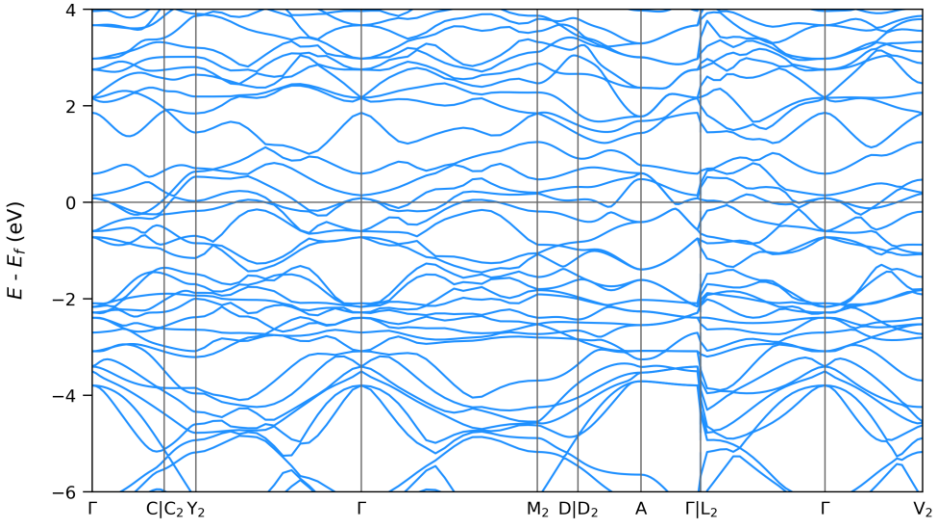

Figure S49. Calculated electronic band structure for $Mo_{4/3}Y_{2/3}AlB_2$ with $C2$ space group symmetry.

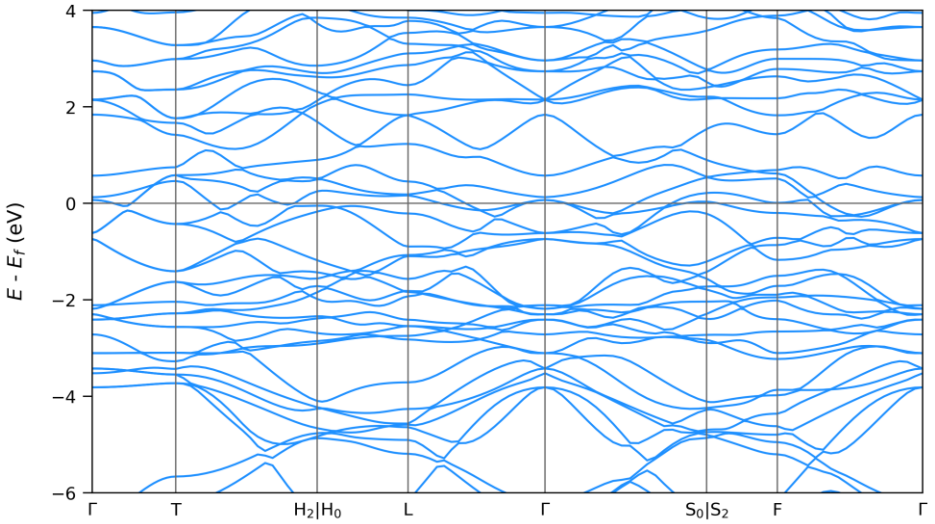

Figure S50. Calculated electronic band structure for $Mo_{4/3}Y_{2/3}AlB_2$ with $R\bar{3}m$ space group symmetry.

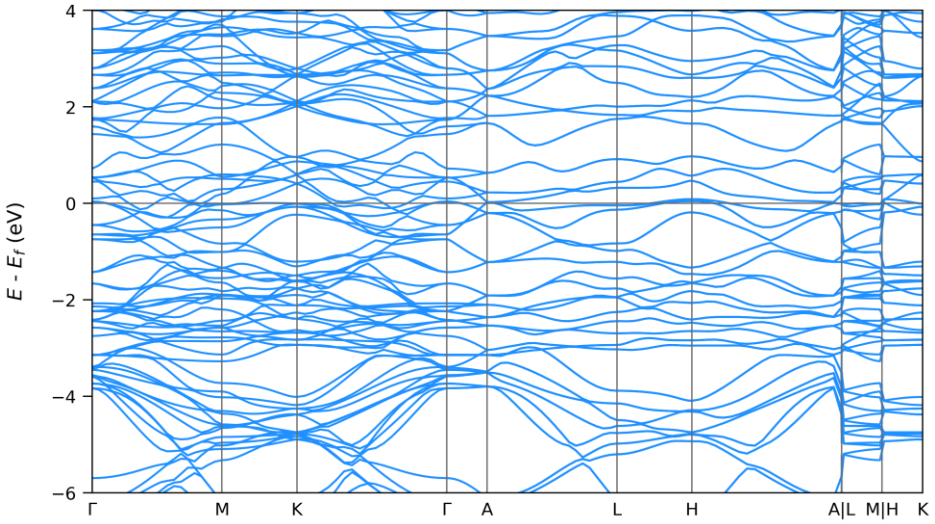

Figure S51. Calculated electronic band structure for $Mo_{4/3}Y_{2/3}AlB_2$ with $P\bar{6}2c$ space group symmetry.

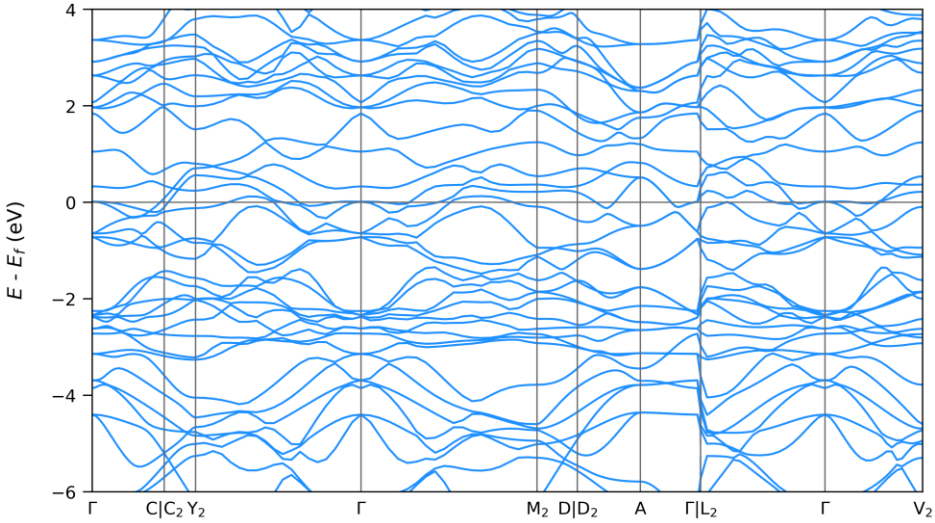

Figure S52. Calculated electronic band structure for $Mo_{4/3}Y_{2/3}GaB_2$ with $C2$ space group symmetry.

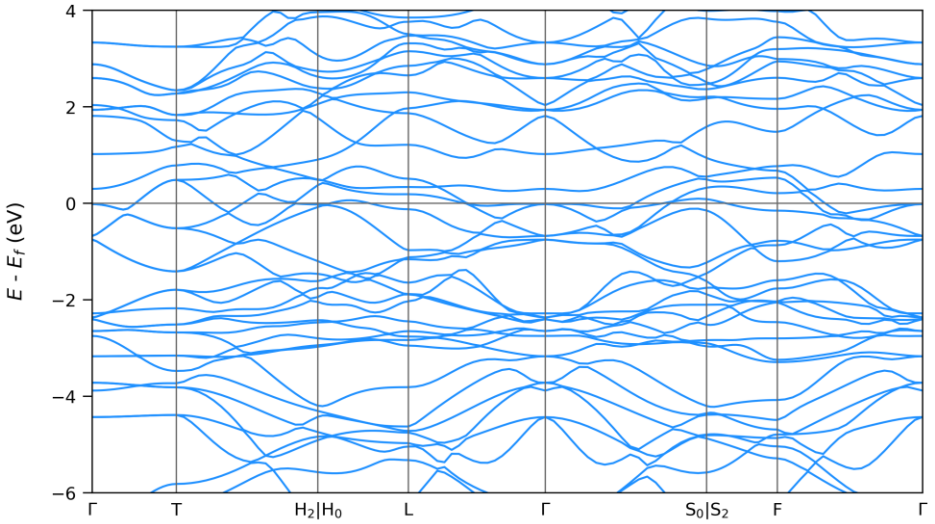

Figure S53. Calculated electronic band structure for $Mo_{4/3}Y_{2/3}GaB_2$ with $R\bar{3}m$ space group symmetry.

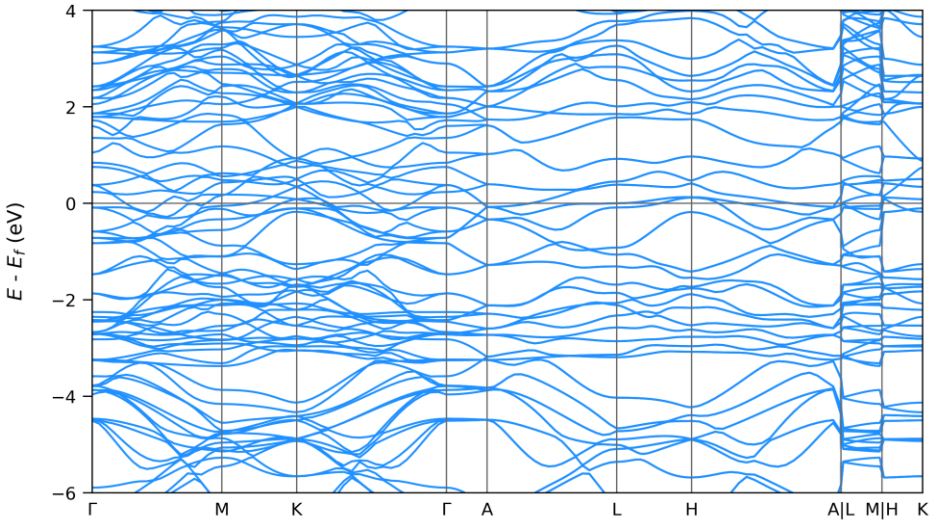

Figure S54. Calculated electronic band structure for $Mo_{4/3}Y_{2/3}GaB_2$ with $P\bar{6}2c$ space group symmetry.

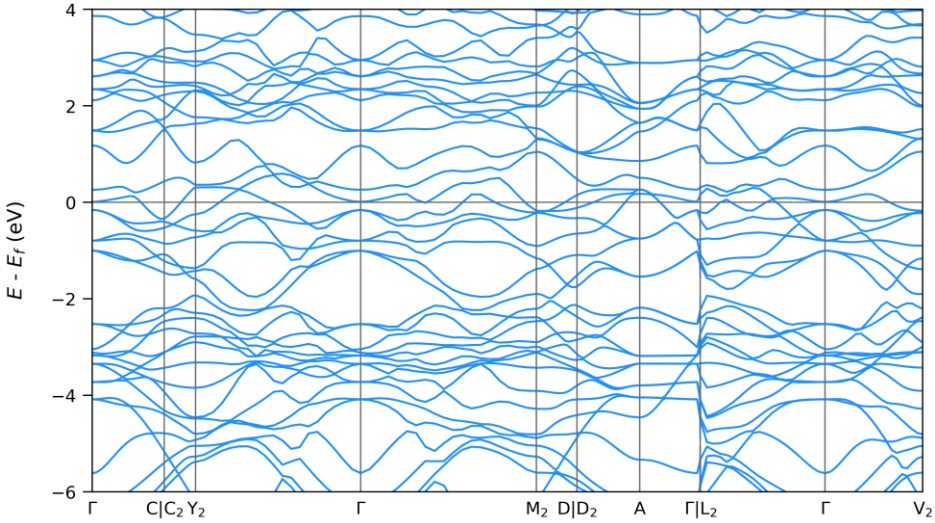

Figure S55. Calculated electronic band structure for $Mo_{4/3}Y_{2/3}SiB_2$ with $C2$ space group symmetry.

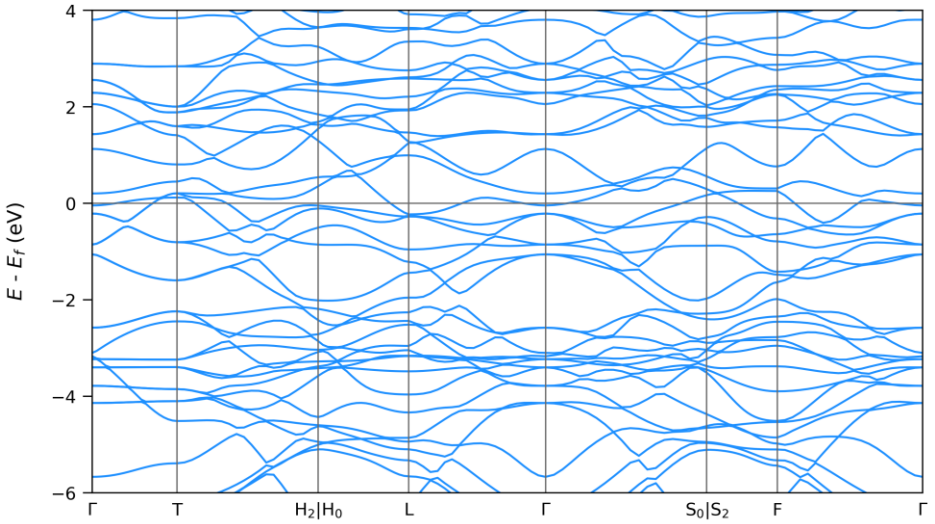

Figure S56. Calculated electronic band structure for $Mo_{4/3}Y_{2/3}SiB_2$ with $R\bar{3}m$ space group symmetry.

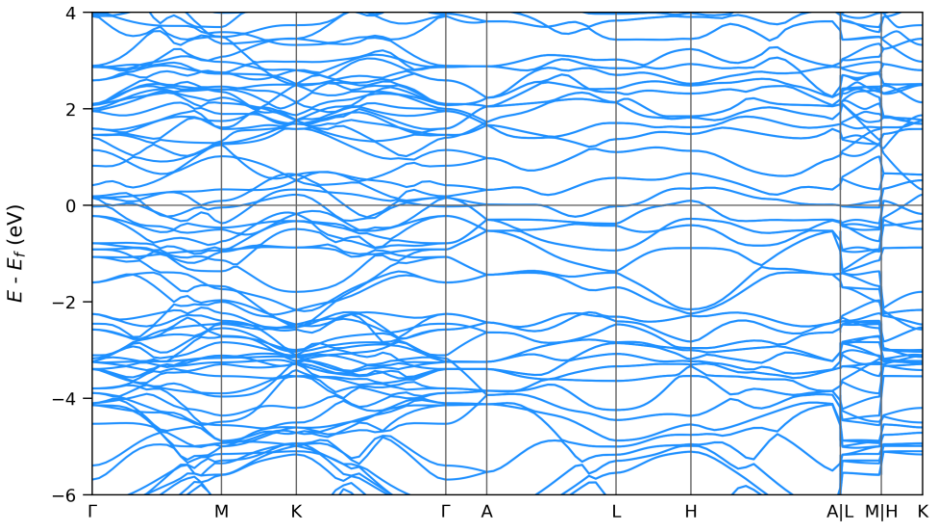

Figure S57. Calculated electronic band structure for $Mo_{4/3}Y_{2/3}SiB_2$ with $P\bar{6}2c$ space group symmetry.

The elastic constants are retrieved using the stress-strain relationship.

$$\boldsymbol{\sigma} = \boldsymbol{C}\boldsymbol{\varepsilon} \tag{Eq. S1}$$

Here $\boldsymbol{\sigma}$ is the stress tensor as obtained from computational output. The strain tensor $\boldsymbol{\varepsilon}$ is applied to transform the shape of the atomic structure. Finally, $\boldsymbol{C}$ is the elastic constant tensor.

$$\boldsymbol{\sigma} = \begin{pmatrix} \sigma_1 \\ \sigma_2 \\ \sigma_3 \\ \sigma_4 \\ \sigma_5 \\ \sigma_6 \end{pmatrix} \quad \boldsymbol{\varepsilon} = \begin{pmatrix} \varepsilon_1 \\ \varepsilon_2 \\ \varepsilon_3 \\ \varepsilon_4 \\ \varepsilon_5 \\ \varepsilon_6 \end{pmatrix} \quad \boldsymbol{C} = \begin{pmatrix} c_{11} & c_{12} & c_{13} & c_{14} & c_{15} & c_{16} \\ c_{12} & c_{22} & c_{23} & c_{24} & c_{25} & c_{26} \\ c_{13} & c_{23} & c_{33} & c_{34} & c_{35} & c_{36} \\ c_{14} & c_{24} & c_{34} & c_{44} & c_{45} & c_{46} \\ c_{15} & c_{25} & c_{35} & c_{45} & c_{55} & c_{56} \\ c_{16} & c_{26} & c_{36} & c_{46} & c_{56} & c_{66} \end{pmatrix} \tag{Eq. S2}$$

The elastic compliances $\boldsymbol{S}$ are the inverse of the elastic constants $\boldsymbol{C}$.

$$\boldsymbol{S} = \begin{pmatrix} s_{11} & s_{12} & s_{13} & s_{14} & s_{15} & s_{16} \\ s_{12} & s_{22} & s_{23} & s_{24} & s_{25} & s_{26} \\ s_{13} & s_{23} & s_{33} & s_{34} & s_{35} & s_{36} \\ s_{14} & s_{24} & s_{34} & s_{44} & s_{45} & s_{46} \\ s_{15} & s_{25} & s_{35} & s_{45} & s_{55} & s_{56} \\ s_{16} & s_{26} & s_{36} & s_{46} & s_{56} & s_{66} \end{pmatrix}; \quad \sum_{\gamma} c_{\alpha\gamma} s_{\gamma\beta} = \delta_{\alpha\beta}; \quad \boldsymbol{C}\boldsymbol{S} = 1 \tag{Eq. S3}$$

In order to use the strain tensor to transform the basis, it is described in the form of a three-dimensional matrix.

$$\boldsymbol{\varepsilon} = \begin{pmatrix} \varepsilon_1 & \varepsilon_6/2 & \varepsilon_5/2 \\ \varepsilon_6/2 & \varepsilon_2 & \varepsilon_4/2 \\ \varepsilon_5/2 & \varepsilon_4/2 & \varepsilon_3 \end{pmatrix} \tag{Eq. S4}$$

In this form, any vector $\boldsymbol{r} = (x, y, z)$ is transformed to $\boldsymbol{r}' = (x', y', z')$ in the following way.

$$\begin{pmatrix} x' \\ y' \\ z' \end{pmatrix} = (\boldsymbol{\varepsilon} + \mathcal{I}) \begin{pmatrix} x \\ y \\ z \end{pmatrix} = \begin{pmatrix} 1+\varepsilon_1 & \varepsilon_6/2 & \varepsilon_5/2 \\ \varepsilon_6/2 & 1+\varepsilon_2 & \varepsilon_4/2 \\ \varepsilon_5/2 & \varepsilon_4/2 & 1+\varepsilon_3 \end{pmatrix} \begin{pmatrix} x \\ y \\ z \end{pmatrix} = \begin{pmatrix} (1+\varepsilon_1)x + \varepsilon_6 y/2 + \varepsilon_5 z/2 \\ \varepsilon_6 x/2 + (1+\varepsilon_2)y + \varepsilon_4 z/2 \\ \varepsilon_5 x/2 + \varepsilon_4 y/2 + (1+\varepsilon_3) \end{pmatrix} \tag{Eq. S5}$$

However, as our *i*-MAB phases of space groups $P\bar{6}2m$, $P\bar{6}2c$ and $R32$ have hexagonal symmetry there are only 6 unique elastic constants.

$$\boldsymbol{C} = \begin{pmatrix} c_{11} & c_{12} & c_{13} & 0 & 0 & 0 \\ c_{12} & c_{11} & c_{13} & 0 & 0 & 0 \\ c_{13} & c_{13} & c_{33} & 0 & 0 & 0 \\ 0 & 0 & 0 & c_{44} & 0 & 0 \\ 0 & 0 & 0 & 0 & c_{44} & 0 \\ 0 & 0 & 0 & 0 & 0 & c_{66} \end{pmatrix} \tag{Eq. S6}$$

In order to obtain these values, we apply the following three strain tensors which we calculate for multiple values of δ. We then approximate the elastic constants from the slope of the stress-strain relations listed below.

$$\boldsymbol{\varepsilon}^1 = \begin{pmatrix} \delta \\ \delta \\ 0 \\ 0 \\ 0 \\ 0 \end{pmatrix} \quad \boldsymbol{\varepsilon}^2 = \begin{pmatrix} \delta \\ -\delta \\ 0 \\ 0 \\ 0 \\ 0 \end{pmatrix} \quad \boldsymbol{\varepsilon}^3 = \begin{pmatrix} 0 \\ 0 \\ \delta \\ \delta \\ \delta \\ \delta \end{pmatrix} \qquad \text{(Eq. S7)}$$

From tensor $\boldsymbol{\varepsilon}^1$:

$$\begin{aligned} \sigma_1 &= (c_{11} + c_{12})\delta \\ \sigma_2 &= (c_{12} + c_{22})\delta \\ \sigma_3 &= (c_{13} + c_{23})\delta \end{aligned} \qquad \text{(Eq. S8)}$$

From tensor $\boldsymbol{\varepsilon}^2$:

$$\begin{aligned} \sigma_1 &= (c_{11} - c_{12})\delta \\ \sigma_2 &= (c_{12} - c_{22})\delta \\ \sigma_3 &= (c_{13} - c_{23})\delta \end{aligned} \qquad \text{(Eq. S9)}$$

From tensor $\boldsymbol{\varepsilon}^3$:

$$\begin{aligned} \sigma_1 &= c_{13}\delta \\ \sigma_2 &= c_{23}\delta \\ \sigma_3 &= c_{33}\delta \\ \sigma_4 &= c_{44}\delta \\ \sigma_5 &= c_{55}\delta \\ \sigma_6 &= c_{66}\delta \end{aligned} \qquad \text{(Eq. S10)}$$

The elastic constants c_{ij} apply to homogenous, monocrystalline structures, but based on these, the polycrystalline elastic constants *B*, *G*, *E* and *v* for a bulk material made up of multiple grains may be calculated as follows, ref [22] in the main article.

In general form the bulk modulus *B* and shear modulus *G* are calculated according to Voigt (B_V and G_V) and Reuss (B_R and G_R).

$$B_V = \frac{(c_{11} + c_{22} + c_{33}) + 2(c_{12} + c_{13} + c_{23})}{9} \qquad \text{(Eq. S11)}$$

$$G_V = \frac{(c_{11} + c_{22} + c_{33}) - (c_{12} + c_{13} + c_{23}) + 3(c_{44} + c_{55} + c_{66})}{15} \qquad \text{(Eq. S12)}$$

$$B_R = \frac{1}{(s_{11} + s_{22} + s_{33}) + 2(s_{12} + s_{13} + s_{23})} \qquad \text{(Eq. S13)}$$

$$G_R = \frac{15}{4(s_{11} + s_{22} + s_{33}) - 4(s_{12} + s_{13} + s_{23}) + 3(s_{44} + s_{55} + s_{66})} \qquad \text{(Eq. S14)}$$

Throughout both the main text of the article, as well as this supplemental, bulk and shear modulus are provided as the Hill averages B_H and G_H.

$$B_H = \frac{B_V + B_R}{2} \qquad \text{(Eq. S15)}$$

$$G_H = \frac{G_V + G_R}{2} \qquad \text{(Eq. S16)}$$

Young's modulus E, or the elastic constant, is derived from bulk and shear modulus according to:

$$E = \frac{9BG}{3B + G} \qquad \text{(Eq. S17)}$$

and the Poisson ratio is defined as

$$\nu = \frac{3B - 2G}{2(3B + G)} \qquad \text{(Eq. S18)}$$

Using the methods above, moduli and Poisson ratio were calculated for selected low-energy symmetries of $Mo_{4/3}Y_{2/3}AB_2$ *i*-MAB phases motivated by their being predicted stable. They are provided in Table S8 and Figure S58. For a given i-MAB composition there are no qualitative differences between different space group symmetries.

Table S8. Calculated moduli and Poisson ratio for $Mo_{4/3}Y_{2/3}AB_2$ with $C2$, $R\bar{3}m$, and $P\bar{6}2c$ space group symmetry and A = Al, Si, Ga.

i-MAB Phase	space group	Moduli (GPa)									Poisson ratio		
		B_V	B_R	B_H	E_V	E_R	E_H	G_V	G_R	G_H	ν_V	ν_R	ν_H
$Mo_{4/3}Y_{2/3}AlB_2$	$C2$ (5)	172	171	171	289	285	287	119	117	118	0.219	0.222	0.220
	$R\bar{3}m$ (166)	172	171	171	291	286	288	119	117	118	0.218	0.221	0.220
	$P\bar{6}2c$ (190)	172	171	171	285	280	282	116	114	115	0.223	0.228	0.226
$Mo_{4/3}Y_{2/3}SiB_2$	$C2$ (5)	197	196	196	291	274	283	116	108	112	0.253	0.267	0.260
	$R\bar{3}m$ (166)	197	196	197	291	275	283	116	109	112	0.253	0.267	0.260
	$P\bar{6}2c$ (190)	196	196	196	287	270	279	114	106	110	0.256	0.270	0.263
$Mo_{4/3}Y_{2/3}GaB_2$	$C2$ (5)	172	171	172	278	272	275	113	110	112	0.231	0.235	0.233
	$R\bar{3}m$ (166)	171	171	171	276	271	273	112	109	111	0.231	0.236	0.234
	$P\bar{6}2c$ (190)	172	171	171	273	267	270	111	108	109	0.235	0.240	0.237

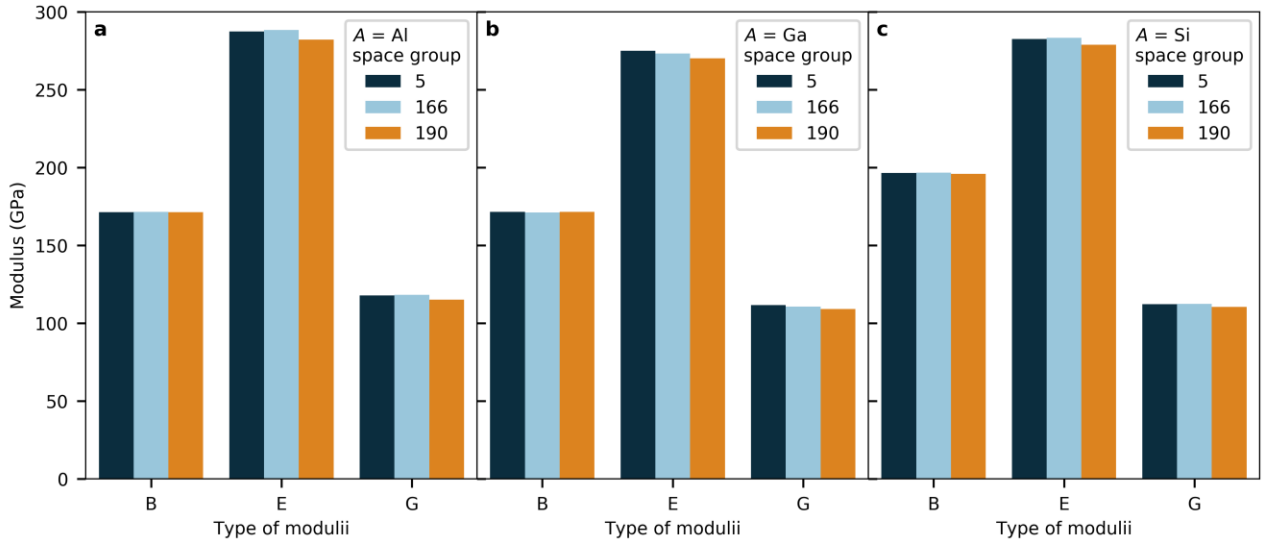

Figure S58. Bulk modulus, B, Young modulus E, and Shear modulus G for $Mo_{4/3}Y_{2/3}AB_2$ with $C2$, $R\bar{3}m$, and $P\bar{6}2c$ space group symmetry for (a) A = Al, (b) A = Ga, and (c) A = Si.

REFERENCES

1. Chaban, N. F.; Kuz'Ma, I. U. B., Ternary systems Cr-Al-B and Mn-Al-B. *Akad. Nauk SSSR Izv. Neorg. Mater.* **1973,** *9*, 1908-1911.
2. Ade, M.; Hillebrecht, H., Ternary Borides Cr_2AlB_2, Cr_3AlB_4, and Cr_4AlB_6: The First Members of the Series $(CrB_2)_nCrAl$ with n = 1, 2, 3 and a Unifying Concept for Ternary Borides as MAB-Phases. *Inorg. Chem.* **2015,** *54* (13), 6122-6135.
3. Chai, P.; Stoian, S. A.; Tan, X.; Dube, P. A.; Shatruk, M., Investigation of magnetic properties and electronic structure of layered-structure borides AlT_2B_2 (T=Fe, Mn, Cr) and $AlFe_{2-x}Mn_xB_2$. *J. Solid State Chem.* **2015,** *224*, 52-61.
4. Becher, H. J.; Krogmann, K.; Peisker, E., Über das ternäre Borid Mn_2AlB_2. *Zeitschrift für anorganische und allgemeine Chemie* **1966,** *344* (3-4), 140-147.
5. Potashnikov, D.; Caspi, E. N.; Pesach, A.; Hoser, A.; Kota, S.; Verger, L.; Barsoum, M. W.; Felner, I.; Keren, A.; Rivin, O., Magnetic ordering in the nano-laminar ternary Mn_2AlB_2 using neutron and X-ray diffraction. *J. Magn. Magn. Mater.* **2019,** *471*, 468-474.
6. Jeitschko, W., The crystal structure of Fe_2AlB_2. *Acta Crystallographica* **1969,** *B25*, 163.
7. Tan, X.; Chai, P.; Thompson, C. M.; Shatruk, M., Magnetocaloric Effect in $AlFe_2B_2$: Toward Magnetic Refrigerants from Earth-Abundant Elements. *J. Am. Chem. Soc.* **2013,** *135* (25), 9553-9557.
8. Wang, J.; Ye, T.-N.; Gong, Y.; Wu, J.; Miao, N.; Tada, T.; Hosono, H., Discovery of hexagonal ternary phase Ti_2InB_2 and its evolution to layered boride TiB. *Nat. Commun.* **2019,** *10* (1), 2284.
9. Hanner, L. A.; Badr, H. O.; Dahlqvist, M.; Kota, S.; Rosen, J.; Barsoum, M. W., Synthesis, Characterization and First Principle Modeling of the MAB Phase Solid Solutions: $(Mn_{1-x}Cr_x)_2AlB_2$ and $(Mn_{1-x}Cr_x)_3AlB_4$. *Mater. Res. Lett.* **2021,** *9* (2), 112-118.
10. Dahlqvist, M.; Tao, Q.; Zhou, J.; Palisaitis, J.; Persson, P. O. Å.; Rosen, J., Theoretical Prediction and Synthesis of a Family of Atomic Laminate Metal Borides with In-Plane Chemical Ordering. *J. Am. Chem. Soc.* **2020,** *142* (43), 18583-18591.
11. Greenwood, N. N.; Earnshaw, A., *Chemistry of the Elements*. 2nd ed.; Butterworth-Heinemann: 1997.
12. Huheey, J. E.; Keiter, E. A.; Keiter, R. L., *Inorganic Chemistry : Principles of Structure and Reactivity*. 4th ed.; HarperCollins: New York, USA, 1993.